UNIVERSIDAD DE CONCEPCIÓN
FACULTAD DE CIENCIAS FÍSICAS Y MATEMÁTICAS
DEPARTAMENTO DE GEOFÍSICA

# SPATIAL VARIABILITY OF SHEAR WAVE VELOCITY: IMPLICATIONS FOR THE LIQUEFACTION RESPONSE OF A CASE STUDY FROM THE 2010 MAULE MW 8.8 EARTHQUAKE, CHILE.

BY

**SEBASTIÁN ALFONSO NÚÑEZ JARA**

Thesis presented to Facultad de Ciencias Físicas y Matemáticas to be eligible for the degree of Master in Geophysics.

January 2024

Concepción, Chile

**Guide Professor:**

Dr. Gonzalo Montalva

**Commitee members:**

Dr. Rodolfo Araya - Dr. Matt Miller - Dr. Marco Pilz

© 2024, SEBASTIÁN ALFONSO NÚÑEZ JARA
Se autoriza la reproducción total o parcial, con fines académicos, por cualquier medio o procedimiento, incluyendo la cita bibliográfica del documento.

UNIVERSIDAD DE CONCEPCIÓN
FACULTAD DE CIENCIAS FÍSICAS Y MATEMÁTICAS
DEPARTAMENTO DE GEOFÍSICA

# VARIABILIDAD ESPACIAL DE LA VELOCIDAD DE ONDA DE CORTE: IMPLICACIONES PARA LA RESPUESTA A LA LICUACIÓN DE UN CASO DE ESTUDIO DEL TERREMOTO DEL MAULE 2010 MW 8.8, CHILE.

POR

**SEBASTIÁN ALFONSO NÚÑEZ JARA**

Tesis presentada a la Facultad de Ciencias Físicas y Matemáticas para optar al grado de Magíster en Geofísica.

Enero 2024

Concepción, Chile

**Profesor Guía:**

Dr. Gonzalo Montalva

**Comision Evaluadora:**

Dr. Rodolfo Araya - Dr. Matt Miller - Dr. Marco Pilz

*Dedicado a Manchina y Capitán.*

# Agradecimientos

En primer lugar, darle las gracias a las personas del Departamento de Geofísica, en especial a la Dra. Carolina Parada, Carla, y Roxana por su incesante apoyo durante todo el magíster. Quiero agradecer enormemente a mi profesor guía Gonzalo Montalva por sus ideas, ánimo y confianza depositada en mí durante todo el posgrado. Al profesor Matt Miller por su incesante disposición en acompañarme durante todo el proceso de tesis y la retroalimentación en la escritura cuando las fechas límites se acercaban peligrosamente. Al profesor Rodolfo Araya por solucionar mis dudas con respecto a los métodos numéricos y por los recursos computacionales que me otorgó para realizar mis cálculos. I also appreciate a lot the support from Dr. Marco Pilz, who always had the willingness to answer my innumerable questions, share good conversations, and host me in the GFZ Potsdam. Muchas gracias al Dr. Andrés Olivar-Castaño por guiarme en la metodología, el apoyo en la escritura y su buena onda siempre.

También agradezco al grupo de Geotecnia del Departamento de Ingeniería Civil de la Universidad de Concepción, en especial a Héctor Saldaña por contribuir esencialmente en esta tesis con su conocimiento, retroalimentación e investigación previa, y a Nicolás Bastías, por siempre ayudarme en las campañas de recolección de datos. Infinitas gracias a mis amistades que me dieron su cariño, buenos momentos y risas, o que incluso me ayudaron en distintas partes de la tesis como la escritura y las simulaciones: Cami, Coto, Denisse, Efra, Honor, Javi, JP, Moi, Pedro, Sali, Sebarra, Sibi, Tomás y Vanessa. Son lo mejor y les extraño caleta. Finalmente, agradecer a mi familia, en especial a Manchina y Capitán, por ser los mejores, quererme mucho y siempre estar para mí cuando lo necesito. Los extraño infinito y ya nos veremos pronto.

Esta tesis fue financiada por la Dirección de Posgrado de la UdeC, el Núcleo Milenio CYCLO, la Iniciativa Científica Milenio NC160025, y los proyectos FONDEF ID1616120157, ID22I10032.

# Resumen

Cuantificar el potencial, la severidad y la extensión de la licuación inducida por terremotos es fundamental para evaluar la amenaza sísmica. Las grandes deformaciones asociadas a este fenómeno pueden ocasionar daños severos en la infraestructura y representar un riesgo para las vidas humanas, como ha quedado evidenciado en numerosos casos históricos y contemporáneos en diversos entornos tectónicos. En esa línea, el modelamiento numérico de casos de estudio, usando modelos constitutivos de suelo y herramientas numéricas de última generación, ha demostrado ser una metodología adecuada para el estudio de la licuación. Ciertamente, las simulaciones numéricas permiten reproducir la respuesta dinámica de suelos licuables en términos de la generación de tensiones efectivas, largas deformaciones, y desplazamientos de suelo de una manera consistente con observaciones experimentales y de campo. Asimismo, se puede estimar el impacto que tiene la variabilidad espacial de las propiedades del suelo en la licuación, puesto que el modelo incorpora naturalmente la respuesta del medio ante la propagación de ondas sísmicas. Con eso en mente, destacamos que el impacto de la variabilidad espacial de la velocidad de onda de corte $V_s$ en la respuesta a la licuación, no ha sido íntegramente evaluado.

En un caso de estudio en el Gran Concepción, Chile, esta investigación se centra en analizar la influencia de la variabilidad espacial de $V_s$ en la respuesta dinámica frente a la licuación. En el sitio, tras el Terremoto del Maule $M_w$ 8.8 de 2010, se evidenciaron efectos de licuación como grietas en el terreno, expulsión de material de suelo, y asentamiento de las estructuras edificadas. Usando perfiles 2D de velocidad generados a partir de perfiles 1D obtenidos con métodos de ruido ambiental, en conjunto con el modelo constitutivo de arenas *PressureDependentMultiYield03*, estudiamos el efecto que tiene la variabilidad espacial de $V_s$ en la generación de presión de poros, asentamientos verticales, y deformaciones de corte y volumétricas. Nuestros resultados indican que un aumento de la variabilidad espacial de $V_s$ reduce las medianas de los asentamientos y deformaciones para las unidades de suelo que exhiben comportamiento no lineal asociado a licuación. Por otra parte, no se observan cambios significativos en la respuesta de las unidades de suelo que no licuan, lo cual implica que la variabilidad

espacial de $V_s$ no influye en el desencadenamiento de la licuación. Inferimos que, cuando existe comportamiento no lineal, un incremento en el amortiguamento de la parte mas superficial del suelo podría ser la explicación de la disminución en la amplitud de deformaciones y asentamientos cuando incrementa la variabilidad de $V_s$.

# Abstract

Assessing the potential, severity, and extent of earthquake-induced liquefaction is paramount for seismic hazard assessment, for the large ground deformations it causes can result in severe damage to infrastructure and pose a threat to human lives, as evidenced by many contemporary and historical case studies in various tectonic settings. In that regard, numerical modeling of case studies, using state-of-the-art soil constitutive models and numerical frameworks, has proven to be a tailored methodology for liquefaction assessment. Indeed, these simulations allow for the dynamic response of liquefiable soils in terms of effective stresses, large strains, and ground displacements to be captured in a consistent manner with experimental and *in-situ* observations. Additionally, the impact of soil properties spatial variability in liquefaction response can be assessed, because the system response to waves propagating are naturally incorporated within the simulations. Considering that, we highlight that the effect of shear wave velocity $V_s$ spatial variability has not been thoroughly assessed.

In a case study in Metropolitan Concepción, Chile, our research addresses the influence of $V_s$ spatial variability on the dynamic response to liquefaction. At the study site, the 2010 Maule $M_w$ 8.8 Earthquake triggered liquefaction-induced damage in the form of ground cracking, soil ejecta, and building settlements. Using simulated 2D $V_s$ profiles generated from 1D profiles retrieved with ambient noise methods, along with a *PressureDependentMultiYield03* sand constitutive model, we studied the effect of $V_s$ spatial variability on pore pressure generation, vertical settlements, and shear and volumetric strains. Our findings indicate that increased $V_s$ variability reduces the median settlements and strains for soil units that exhibit liquefaction-like responses. On the other hand, no significant changes in the dynamic response are observed in soil units that exhibit non-liquefaction behavior, implying that the triggering of liquefaction is not influenced by spatial variability in $V_s$. We infer that when liquefaction-like behavior is triggered, an increase of the damping at the shallowest part of the soil domain might be the explanation for the decrease in the amplitude of the strains and settlements as the degree of $V_s$ variability increases.

# Contents

**Resumen** **ii**

**Abstract** **iv**

**1 Introduction** **1**
1.1 Hypothesis . . . 5
1.2 Main Objective . . . 5
1.3 Specific Objectives . . . 6

**2 Theory** **7**
2.1 Retrieving dispersion curves from ambient noise data . . . 7
2.2 Retrieving ground profiles from dispersion curves . . . 9

**3 Background and Methods** **11**
3.1 The Los Presidentes case study . . . 11
3.2 Data acquisition and ground profile computation . . . 14
3.3 Retrieval of the site velocity structure . . . 16
3.4 Numerical Model Setup . . . 20

**4 Results** **26**
4.1 Benchmark Simulation . . . 27
4.2 Assessing the effect of $V_s$ variability on key dynamic properties . . . 29

**5 Discussion** **35**
5.1 Further Work . . . 38

**6 Conclusion** **39**

**References** **41**

**Supplemental Material** **53**

S1 Scientific Production . . . . . 53
S2 Supplemental Figures . . . . . 54

# List of Figures

3.1.1 Satellite View of Metropolitan Concepción. Peak ground acceleration (PGA) color-coded circles show sites where surficial evidence of liquefaction was reported (Montalva et al., 2022). The PGAs were computed with Montalva et al. (2017) Ground Motion Prediction Equation. The dashed light-green circle encapsulates our study site, Los Presidentes. The cyan cross depicts the location of strong-motion station CCP, from which the earthquake ground motion was deconvolved to use as input for the site response analysis. . . . . 13
3.1.2 Summary of the damages at the Los Presidentes site. Panel (a): Site boundary, damages in the form of ground cracks and boil ejecta. only buildings A, B, C, and D are labeled because the northernmost ones were not built at the time of the earthquake. Panel (b): A LiDAR image with the liquefaction-induced building settlements measured at the site (Robert Kayen, personal communication). Panels (c)-(d): Evidence of soil ejecta at the northeastern corner and inside the residential complex, respectively. Panel (e): Evidence of ground cracking between buildings A and C. Figure was extracted from Saldaña Sotelo (2023); Saldaña et al. (2023), and references therein. . . . . 14
3.2.1 Panel (a): Schematic view of the study site. Magenta triangles depict the positions of seismic sensors, black lines connecting them show the station pairs from which dispersion curves shown in (b) were retrieved. The dashed red line represents the T-T' cross-section employed in the numerical model. Panel (b): Distribution of all Rayleigh Wave dispersion curves across the study site. . . . . 16

3.3.1 Top panels: The ground profiles inverted from the dispersion curves displayed in the lower panels. Grey profiles show the lowest misfit solution for each seed. The red profile is the lowest-misfit solution for all seeds. The dashed blue line represents the logarithm of the standard deviation of $V_s$. Lower panels: Dispersion curve fit (dotted black line) by each ground profile. Colors represent the same as at the top panels. . . . . 19
3.3.2 The velocity structure of the site calculated by the weighting scheme. Panels (a)-(c): Average $V_s$ structure at depths of (0-10 [m]), (10-20 [m]) and (20-30[m]), respectively. In (a)-(c), the X and Y coordinates are within the coordinate system of Fig. 3.2.1a. Panel (d): Distribution of ground profiles averaged on each grid to obtain the weighted ground profile. Panel (e): The weighted ground profiles of all grids. Three representative profiles of different ground conditions are depicted with red, blue, and black lines. The red velocity profile, which represents free-field conditions, is used for the ESSRAs. Panels (f)-(g): Black and orange ground motion and their Fourier spectrums depict the CCP EW station recording and its deconvolution to 50 meters depth, respectively. . . . . 20
3.4.1 Benchmark finite element model realization of the T-T' cross-section defined in Fig. 3.2.1. Top panel: $V_s$ random field obtained using $\sigma_{ln,v_s} = 0.075$. Free-field columns at the lateral boundaries are depicted in thick black rectangles. The red arrows start and end at the main and constraint nodes, respectively. Input ground motion is applied at the green node in the lower-left corner. Base nodes (blue) are constrained to the green node. The recorder nodes at a depth of three meters are depicted as magenta triangles and are further analyzed in Fig.4.2.1. Lower panel: $D_r$ structure of the cross-section (Saldaña et al., 2023). 24

4.1.1 Maximum shear strain (a), volumetric strain (b), excess pore-water pressure ratio (c), horizontal acceleration (d), and settlements (e) for the benchmark model realization shown in Fig. 3.4.1. The magenta numbered circles represent the locations of the three nodes depicted in Fig. 4.1.2. . . . . 28
4.1.2 Recorder acceleration, excess pore-water pressure, and stress-strain time series of the numbered nodes of Fig. 4.1.1. Top panel: Node 1. Middle panel: Node 2. Bottom panel: Node 3. The time series' black, red, and blue color codes represent the first 15 seconds of motion, from 15 to 75 seconds, and from 75 to the end of motion. . . . . 29

4.2.1 Median of the max. shear strain (a); max. volumetric strain (b); max. PWP ratio (c); and vertical settlements (d); at different levels of $\sigma_{ln,v_s}$ across the T-T' cross-section. Nodes are located at a depth of 2 meters. Thick black vertical line divides the western from eastern nodes. Thick red vertical lines depict the location of the western and eastern nodes analyzed in Figs. 4.2.2 and Fig. S2.5. Horizontal black lines near the x-axis represent the locations of towers A and B relative to the cross-section. . . . . 32
4.2.2 All simulations of shear strain (a), volumetric strain (b), vertical displacement (c), and excess pore-water pressure ratio (d) time series computed for the node at the western node at position $x = 54$ and depth of 2 meters, depicted in Fig. 4.2.1. Color-coded time series represent the median time series at different levels of $\sigma_{ln,v_s}$. Black curves represent all simulations' 20-th and 80-th percentile time series. 33
4.2.3 The same parameters, represented in the same colors, as for Fig. 4.2.2, but this time for the eastern node at position $x = 86$ and depth of 2 meters. . . . . 34

S2.1 The same parameters, represented in the same colors, as for Fig. 4.2.1, but this time for a depth of 3 meters. . . . . 54
S2.2 The same parameters, represented in the same colors, as for Fig. 4.2.1, but this time for a depth of 4 meters. . . . . 54
S2.3 The same parameters, represented in the same colors, as for Fig. 4.2.2, but this time for the western node at position $x = 54$ at a depth of 3 meters. . . . . 55
S2.4 The same parameters, represented in the same colors, as for Fig. 4.2.2, but this time for the western node at position $x = 54$ at a depth of 4 meters. . . . . 56
S2.5 The same parameters, represented in the same colors, as for Fig. 4.2.2, but this time for the eastern node at position $x = 86$ and depth of 2 meters. . . . . 57

# List of Tables

3.4.1 Joint ground profile obtained by merging the median profile from this work and the uppermost two layers of the profile derived in Inzunza et al. (2019). . . . . 25
3.4.2 PressureDependentMultiYield03 model parameters employed in this research. . . . . 25

5.0.1 Minimum, average, and maximum settlements (in centimeters) obtained at tower A (node $x = 38$) for different levels of $V_s$ spatial variability. . . . . 37
5.0.2 Minimum, average, and maximum settlements (in centimeters) obtained at tower B (node $x = 78$) for different levels of $V_s$ spatial variability. . . . . 38

# Chapter 1

# Introduction

Earthquake-induced liquefaction occurs when granular soils, frequently loose to medium-dense saturated sands, exhibit a significant loss of strength and stiffness and start behaving as a liquid. The large ground deformations and damages resulting from liquefaction have been well-documented in recent case histories. Notable examples include the 2010 Maule Chile earthquake $M_w$ 8.8 (Bray et al., 2012; Verdugo and González, 2015), the 2010-2011 Canterbury earthquake sequence in New Zealand (maximum magnitude $M_w$ 7.1, Green et al., 2014; Van Ballegooy et al., 2014), the 2012 Emilia Earthquake sequence in Northern Italy (maximum magnitude $M_w$ 6.1, Alessio et al., 2013), and the recent Kahramanmaras earthquake sequence (maximum magnitude $M_w$ 7.8, Baser et al., 2023; Taftsoglou et al., 2023). Although these earthquakes varied in magnitude, tectonic setting, and resultant ground motion intensities, they produced moderate to severe liquefaction-induced damage in the form of sand boils, building and ground settlements, ground cracking, soil ejecta, and lateral spreading. Furthermore, these effects occurred within bounds defined by an empirical relationship between magnitude and maximum fault distance at which liquefaction was reported (Hu, 2023).

To comprehend the mechanisms behind the observed ground deformations, researchers conduct backanalyses of liquefaction case studies. This involves collecting geotechnical

and geophysical data and then utilizing empirical or analytical methods to establish a connection between predictions and observations. This is a challenging task due to the complex and nonlinear nature of liquefaction, which involves significant deformations and fluid flow. Additionally, *in-situ* data is often sparse and may not accurately reflect the spatial variability in the site conditions, the input ground motion can only be approximated to a limited extent, and predictor models may not be tailored for reproducing the diverse range of surficial manifestations of liquefaction. The most widely known methodology for achieving this goal, the *simplified procedure* (Seed and Idriss, 1971; Youd and Idriss, 2001; Boulanger and Idriss, 2014), comprises a collection of semi-empirical relationships that proxy the seismic load and soil strength for a given layer with its geomechanical properties derived from *in-situ* measurements. However, the assumption of free-field conditions (i.e., the absence of structural load) and 1D vertical stratification of isolated soil layers falls short in accurately reproducing the dynamic response of the media, causing discrepancies between observations and predicted outcomes as evidenced in recent case studies (Dashti and Bray, 2013; Luque and Bray, 2017; Cubrinovski et al., 2019; Hutabarat and Bray, 2021).

On the other hand, Effective Stress Site Response Analyses (ESSRAs) have been demonstrated to be a more suitable alternative than the *simplified procedure* for evaluating liquefaction response. In this approach, the seismic load is integrated as equivalent forces applied at the boundaries of a defined soil domain, and the soil media is modeled as a two-phase material (i.e., solid and fluid). By using a proper constitutive model, the wave propagation problem is solved under undrained conditions to reproduce the nonlinear elastoplastic stress-strain response, pore-water pressure generation, and post-shaking dissipation generated by an earthquake (Popescu et al., 2006). ESSRAs of case histories have been able to successfully reproduce the pore-pressure build-up, flow patterns, and large shear and volumetric strains that lead to ground deformations consistent with surficial evidence (Bray and Luque, 2017; Luque and Bray, 2017; Bassal and Boulanger, 2021; Pretell et al., 2021; Qiu et al., 2023; Saldaña et al., 2023). Furthermore, parametric studies have been conducted to evaluate the influence of soil properties and ground motion intensity variability on liquefaction response (Popescu et al., 1997, 2005; Boulanger and Montgomery, 2016;

Montgomery and Boulanger, 2017).

Under the assumption that the constitutive model, the earthquake loading, and the numerical framework to perform the simulations are well defined, the soil domain must be sufficiently characterized to evaluate the liquefaction response of documented case histories. Certainly, research indicates that identifying the strength, extent, and behavior type of geotechnical units is pivotal for understanding the observed deformation patterns (Cubrinovski et al., 2019; Luque and Bray, 2020; Bassal and Boulanger, 2023). Geotechnical vertical soundings, such as the Standard Penetration Test (SPT) and the Cone Penetration Test (CPT), are commonly carried out for the characterization of the soil structure because the measurements provided by these tests correlate to essential parameters that control the liquefaction potential of the soil, such as the relative density ($D_r$), soil behavior type ($I_c$), and hydraulic conductivity ($k$). Shear-wave velocity $V_s$ measurements are also commonly conducted to constrain the soil's elastic properties. This parameter is defined as

$$V_s = \sqrt{\frac{G_{max}}{\rho}}, \tag{1.0.1}$$

where $G_{max}$ is the shear modulus at small strains and $\rho$ is the density of the media. Intuitively, $V_s$ is a measurement of the stiffness of the soil and its ability to undergo shear strains. This parameter can be determined through invasive methods, and non-invasive methods based on the propagation of surface waves generated by passive or active sources. It has been shown that, despite the higher resolution of the invasive methods, the precision of both methods is comparable (Garofalo et al., 2016).

The use of shear-wave velocity as a proxy for soil response to liquefaction has a long-standing history: $V_s$ depends on the overburden effective stress and the void ratio of the soil (Kayen et al., 2013). Liquefaction potential is highly sensitive to the void ratio, as soils with a high void ratio have the ability to store more pore-water pressure. With that in mind, in the context of the *simplified procedure*, experimental and *in-situ* data have been used to derive deterministic and probabilistic empirical relationships between $V_s$ and the cyclic resistance and stress ratio of soils (Tokimatsu

and Uchida, 1990; Andrus and Stokoe II, 2000; Zhou and Chen, 2007; Kayen et al., 2013). In recent years, data-driven methods based on artificial intelligence have been developed for predicting liquefaction (Zhang et al., 2021; Zhang and Wang, 2021). The performance of these methods has significantly improved when coupling geotechnical data (CPT and SPT) with $V_s$ measurements. In the context of site response analyses, $V_s$ is an essential parameter for wave propagation problems because it governs seismic wave amplitude and constrains the stress-strain response of soil units.

Of particular interest for this research, the influence of $V_s$ spatial variability on ground motion has been highlighted by various studies. In general, the $V_s$ structure of a site is three-dimensional due to the presence of basins, topographic irregularities, and inherent soil variability. Whether the site response may be accurately represented as 2D or 1D must be assessed from case to case (Thompson et al., 2012; Pilz and Cotton, 2019; Tao and Rathje, 2020; Pilz et al., 2021; Hallal and Cox, 2023). At shallow depths ($< 50$m), linear elastic and viscoelastic 2D site response analyses have shown that increasing the degree of spatial variability in $V_s$ correlates with an increased ground motion variability, especially at frequencies higher than the resonant frequency of the soil (El Haber et al., 2019; Huang et al., 2021; de la Torre et al., 2022a). This can be attributed to the frequency-dependent wave attenuation (Aki, 1980; Assimaki, 2004). Nonlinear site response analyses have also been conducted to assess the effect of $V_s$ spatial variability using a total stress formulation (Assimaki et al., 2003). In this case, the hysteretic loops of the soil do not follow the same path during loading and unloading, implying energy dissipation and shear modulus degradation, which in turn leads to increased motion damping when the soil is subjected to higher strains (Hashash and Park, 2001, 2002). Keeping this in mind, to the best of our knowledge, there is a limited exploration of the influence of $V_s$ spatial variability in liquefaction response through nonlinear effective stress analyses.

This research aims to assess the effect of $V_s$ spatial variability in liquefaction triggering, stress-strain response, and liquefaction-induced settlements. To do so, we consider a residential area in Metropolitan Concepción, Chile, where a variable response to

liquefaction was reported in the frame of the 2010 $M_w$ 8.8 Maule Earthquake, which has already been thoroughly studied and geotechnically characterized (Bray et al., 2012; Verdugo and González, 2015; Montalva et al., 2022; Saldaña et al., 2023). Using seismic arrays deployed within the site, we retrieve several $V_s$ profiles from ambient noise data using the SPatial AutoCorrelation (SPAC) technique (Aki, 1957; Chávez-García et al., 2005; Tsai and Moschetti, 2010). This allows us to identify key soil profiles consistent with the site characteristics. We then generate 2D heterogeneous $V_s$ model realizations from the soil profiles, using correlated random fields at different levels of variance. This process is similar to approaches used in non-liquefaction site response analyses (Assimaki et al., 2003; El Haber et al., 2019; de la Torre et al., 2022a,b). Finally, we perform ESSRA, using each model realization as an input, to assess the impact of different levels of variance on the dynamic response of the soil in terms of excess pore water pressure, generated shear and volumetric strains, and vertical settlements.

## 1.1 Hypothesis

$V_s$ spatial variability influences liquefaction response in terms of excess pore-water pressure generation, shear and volumetric strains, and vertical settlements because of the exhibited nonlinear response of saturated soils due to strong earthquake motions. We infer that an increase of the shear-strain dependent soil damping with increasing degree $V_s$ spatial variability is the principal factor that explains this behavior.

## 1.2 Main Objective

To assess the effect of $V_s$ spatial variability in liquefaction response, by performing effective stress site response analyses at a residential site that exhibited major liquefaction damage in the context of the 2010 $M_w$ 8.8 Maule Earthquake.

## 1.3 Specific Objectives

- To conduct geophysical surveys at the site of the study in order to record the microtremor wavefield.

- To retrieve the study site shallow velocity structure from the recorded data using seismic interferometry principles.

- To generate spatially heterogeneous $V_s$ soil domains from the known site velocity structure, using Gaussian correlated random fields.

- To perform site response analyses with the $V_s$ 2D models coupled with a proper site geotechnical characterization, constitutive model, numerical model framework, and boundary conditions.

- To compare the simulation results at different degrees of $V_s$ spatial variability in terms of pore-water pressure generation, shear strains, volumetric strains, and vertical settlements.

# Chapter 2

# Theory

## 2.1 Retrieving dispersion curves from ambient noise data

The noise wavefield refers to the combination of seismic waves caused by ambient vibrations of both natural and human origin, such as tides, oceanic waves, meteorological phenomena, heavy machinery, and vehicles (Asten and Henstridge, 1984; Bonnefoy-Claudet et al., 2006). This wavefield is primarily composed of surface waves (Bonnefoy-Claudet et al., 2006; Tsai and Moschetti, 2010; Díaz et al., 2017). The dispersive nature of the surface waves allows us to illuminate the Earth's internal structure through the seismic interferometry technique (Curtis et al., 2006). Under the assumption that the noise wavefield is diffuse (i.e., waves with uncorrelated random amplitudes and phases propagate in all directions Weaver 1982; Lobkis and Weaver 2001), the Green's Function and the group or phase velocity dispersion curve between two receivers can be calculated by averaging the correlograms over time (Shapiro and Campillo, 2004; Wapenaar et al., 2010). The widespread success of ambient seismic noise methodologies in recent years has demonstrated their effectiveness in a variety of applications, ranging from soil structure characterization to lower crust/upper mantle tomographic models (e.g., Shapiro et al. 2005; Ritzwoller et al. 2011; Ward et al. 2013;

Inzunza et al. 2019). The bandwidth of the retrieved dispersion curves is primarily constrained by instrumental characteristics, the interstation distance between the receivers, and the deployment time of the seismic array. The number of stacked correlograms, whose duration is frequency-dependent, increases the signal-to-noise ratio (Bensen et al., 2007). In fact, for shallow imaging (i.e., $< 100$ meters), recording for a few hours should suffice (e.g., Picozzi et al. 2009; Pilz et al. 2012). On the other hand, researchers have stacked years of data to obtain dispersion curves for deeper explorations (e.g., Ward et al. 2013).

The aforementioned approach is based on time-domain cross-correlation. However, a similar method, called SPatial AutoCorrelation (SPAC, Aki 1957), states that if the noise wavefield is stochastic and stationary in space and time, the azimuthal average of the cross-correlation in the frequency domain (i.e., the cross-coherence CC) for a fixed distance $r$ at frequency $\omega$ is related to the Rayleigh wave phase velocity $c(\omega)$ by

$$\bar{\rho}(r,\omega) = AJ_0\left(\frac{\omega r}{c(\omega)}\right), \tag{2.1.1}$$

where $J_0$ represents the zero-th Bessel function of the first kind, and $A$ is an amplitude factor that considers attenuation and normalization errors in the cross-coherence (e.g., Menke and Jin 2015). It is noteworthy that the azimuthal average can be replaced by the time average if we consider that the noise wavefield is diffuse (Aki, 1957; Chávez-García et al., 2005). This implies that the cross-correlation and SPAC methods are equivalent (Tsai and Moschetti, 2010). With that in mind, the time-averaged cross-coherence is defined as (Ohori et al., 2002; Wapenaar et al., 2010; Xu et al., 2021)

$$\rho_{ij}(\omega) = \left\langle \frac{\Re\left(S_{ij}(\omega)\right)}{\sqrt{S_{ii}\left(\omega\right) S_{jj}\left(\omega\right)}} \right\rangle, \tag{2.1.2}$$

where $\Re\left(S_{ij}\right)$ is the real part of the cross power spectral density (PSD) between station pair $i$ and $j$, $S_{ii}$ and $S_{jj}$ are the individual PSDs, and the $\langle\cdot\rangle$ operator denotes averaging over time segments. For each pair of simultaneous recordings, the CC is calculated with eq. (2.1.2), and substituted into eq. (2.1.1). It is clear from these equations that the relationship between the data and the phase velocity is nonlinear.

Still, the dispersion curve $c(\omega)$ can be retrieved through the zero-crossings (Ekström et al., 2009; Ekström, 2014) or by fitting a Bessel function to the CC waveform (e.g., Menke and Jin, 2015; Pilz et al., 2017; Olivar-Castaño et al., 2020).

## 2.2 Retrieving ground profiles from dispersion curves

The relationship between the dispersion curve and a one-dimensional ground profile is also nonlinear. Furthermore, the dispersion curve includes contributions from both fundamental and higher modes, which cannot be trivially separated. The curve that is composed of this superposition of modes is known as the apparent dispersion curve. This curve is related to each mode through their respective medium response functions (Harkrider, 1964; Tokimatsu et al., 1992; Ohori et al., 2002). Therefore, the nonlinear inverse problem relating the apparent dispersion curve and the ground profile can be solved using adequate methods, such as the simplex downhill method (Nelder and Mead, 1965) or a genetic algorithm (Yamanaka and Ishida, 1996; Parolai et al., 2005).

The genetic algorithm employed in this research is a nonlinear, partially probabilistic approach that aims to explore the entire parameter space in order to find the optimal solution (i.e., the space within the predefined lower and upper bounds for density and P-S wave velocity). Since each inversion is defined by a random seed, all resulting solutions are unique, even if they start with the same parameterization. Consequently, there are two significant issues regarding the inverse problem solution and parameterization: the non-uniqueness of the solution and how well it is constrained by the available data. The first issue implies that many different ground profiles may fit the data reasonably well, making it difficult to determine a single 'true' solution. The second issue highlights the limitations of dispersion curve data and how this data constrains each layer's thickness and the maximum depth exploration. A layering-by-ratio scheme was designed to address these issues (Cox and Teague, 2016; Vantassel and Cox, 2021). This approach allows for the exploration of various parameterizations, with different numbers of layers, in order to determine the optimal number of layers that suitably fit the data, preventing over or under-parameterization. Moreover, it

ensures that no layers begin below the wavelength-defined spatial resolution. The best-constrained solution can be selected by minimizing the misfit between the data and the prediction, and a measurement of the inter-parameterization uncertainty can be obtained from the N-lowest misfit solutions (e.g., N = 10, 100).

# Chapter 3

# Background and Methods

## 3.1 The Los Presidentes case study

The megathrust 2010 $M_w$ 8.8 Maule Earthquake that struck South-Central Chile ruptured a mature seismic gap that was quiescent since the 1835 $M_w$ 8.5 Concepción Earthquake (Campos et al., 2002; Ruegg et al., 2009; Moreno et al., 2010; Lay, 2011). The rupture propagated bilaterally north and south of the epicenter, covering an along-strike length of around 500 kilometers. The damages reported spanned from the city of Valparaíso (33.0°S) to Temuco (38.7°S) (Bray et al., 2010; Assimaki et al., 2012). The city of Concepción (Fig. 3.1.1), located in South-Central Chile, experienced particularly strong ground motions. This behavior was attributed to site and basin effects that amplified the seismic motions within the city (Assimaki et al., 2012; Montalva et al., 2016; Inzunza et al., 2019). Particularly, earthquake-induced liquefaction was reported throughout the city with varying levels of severity, including sediment ejecta, lateral spreading, flow failure, excessive settlements, surface cracks, and structural damage (Bray et al., 2010, 2012; Verdugo and González, 2015; Montalva et al., 2022).

Fig. 3.1.2a shows a satellite view of our case study area. At the time of the

2010 earthquake, there were four eight-story buildings on the site (towers A, B, C, and D); currently, there are six of them. Surficial evidence of liquefaction was reported on the site in the form of sediment ejecta (brown shapes in Fig. 3.1.2a and 3.1.2c-d), ground cracking (orange lines in Fig. 3.1.2a and 3.1.2e), and building settlements Bray et al., 2010, 2012). A Light Detection and Ranging (LiDAR) image (Fig. 3.1.2b) revealed that tower A experienced settlements ranging from 6.9 cm to 34.5 cm, while tower B experienced settlements ranging from 7.6 cm to 10.7 cm (Robert Kayen, Personal Communication). These large settlements caused extensive structural damage, leading to the demolition of both towers in 2013; they were subsequently reconstructed between 2016 and 2018. The other two towers, C and D, only experienced minimal settlements. Outside of the studied area, no evidence of liquefaction was reported. In this study, we have focused our region of interest to the area between buildings A and B (Fig. 3.2.1a). Five geotechnical tests were conducted in this region - two SPT, and three CPT boreholes (cyan stars in Fig. 3.2.1a). A comprehensive geotechnical characterization of the site is described in Saldaña et al. (2023).

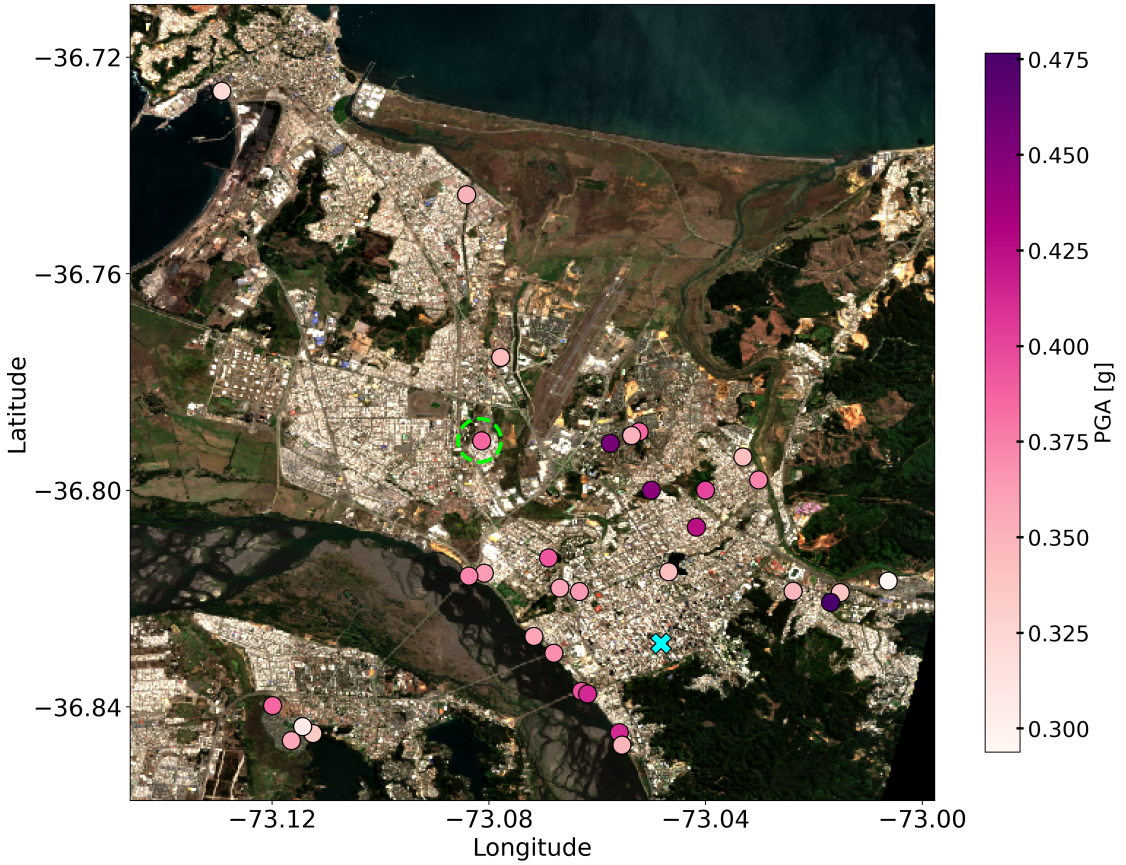


**Figure 3.1.1:** Satellite View of Metropolitan Concepción. Peak ground acceleration (PGA) color-coded circles show sites where surficial evidence of liquefaction was reported (Montalva et al., 2022). The PGAs were computed with Montalva et al. (2017) Ground Motion Prediction Equation. The dashed light-green circle encapsulates our study site, Los Presidentes. The cyan cross depicts the location of strong-motion station CCP, from which the earthquake ground motion was deconvolved to use as input for the site response analysis.

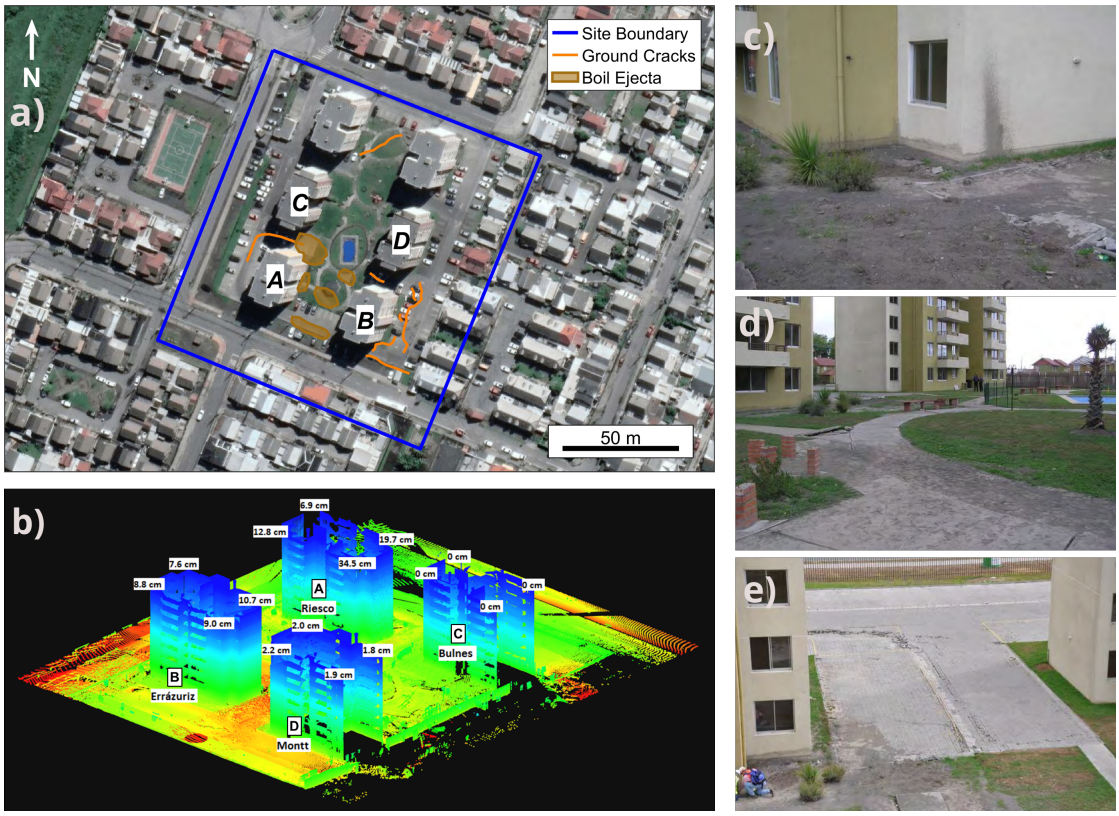


**Figure 3.1.2:** Summary of the damages at the Los Presidentes site. Panel (a): Site boundary, damages in the form of ground cracks and boil ejecta. only buildings A, B, C, and D are labeled because the northernmost ones were not built at the time of the earthquake. Panel (b): A LiDAR image with the liquefaction-induced building settlements measured at the site (Robert Kayen, personal communication). Panels (c)-(d): Evidence of soil ejecta at the northeastern corner and inside the residential complex, respectively. Panel (e): Evidence of ground cracking between buildings A and C. Figure was extracted from Saldaña Sotelo (2023); Saldaña et al. (2023), and references therein.

## 3.2 Data acquisition and ground profile computation

In the frame of this study, we conducted five geophysical surveys from November 2021 to December 2022. Three-component high-frequency seismic Tromino® instruments, with a sampling rate of 512 Hz, were deployed at the study site to record the ambient seismic wavefield at a total of 50 station positions (magenta triangles in Fig. 3.2.1a). The instruments were configured to record synchronously for a duration of

approximately 40 minutes at each position. For each pair of simultaneous recordings (black lines in Fig. 3.2.1a), the CC was calculated with eq. (2.1.2) using the Welch Method (Welch, 1967). This method involves computing periodograms from detrended segments of 60 seconds in length, with a 50% overlap between segments. Additionally, a 5% cosine taper was applied to both ends of each segment, followed by a one-bit normalization filter. This procedure reduces spectral leakage and increases the signal-to-noise ratio (Bensen et al., 2007). Finally, the CC was smoothed using a moving-average filter and substituted into equation (2.1.1). The lower and upper phase velocity limits for the solution were set to 100$[m/s]$ and 400$[m/s]$, respectively, based on results from previous surveys (Montalva et al., 2022; Saldaña et al., 2023). We defined the minimum resolvable wavelength, $\lambda_{min}$, as half the interstation distance $(r/2)$. Due to the different interstation distances, we manually defined the frequency band for the 198 CC waveforms produced. Furthermore, we conducted a visual inspection of the resulting dispersion curves, obtained using the methodology of Menke and Jin (2015), discarding any curves that fit the CC waveforms poorly and outliers corresponding to geologically-implausible interpretations. A subset of 123 curves, presented in Fig. 3.2.1b, aligned with the aforementioned criteria. The minimum and maximum velocities are 116 and 320 $[m/s]$, respectively, while the frequency range spans from 2.85 to 25 Hz. The majority of dispersion curves fall within the $6 - 16$ Hz frequency band, and are representative of very soft, shallow conditions. Subsequently, each dispersion curve is transformed from linear-frequency to the log-wavelength domain. Given that the variation of phase velocity as a function of wavelength is less than as a function of frequency, this transformation reduces the gap between points in the dispersion data without needlessly increasing the number of samples (Vantassel and Cox, 2021).

We inverted ground profiles for each dispersion curve using a generic algorithm (Yamanaka and Ishida, 1996; Parolai et al., 2005) with parameterizations consisting of 3, 4, and 5 layers for each curve, with the deepest layer representing the half-space base. The $V_s$ lower and upper bounds of each layer (regardless of their depth) were set to depend on the lower and upper values of the dispersion curve, ranging from approximately 100 $m/s$ to 350 $m/s$ for the upper sedimentary layers and up to 450

$m/s$ for the half-space layer. As the generic algorithm is part-probabilistic, each dispersion curve was inverted using 12 seeds, resulting in a total of 36 inversions for each curve considering the different numbers of layers used. Then, through visual inspection of the ground profiles and their goodness-of-fit to the data, we determined the number of layers most adequate for each curve and identified the representative ground profile as the one exhibiting the lowest misfit with respect to the dispersion curve. Furthermore, from the 12 solutions, we estimated the inter-model uncertainty by calculating $\sigma_{ln,v_s}$, representing the logarithm of the standard deviation of the velocity.

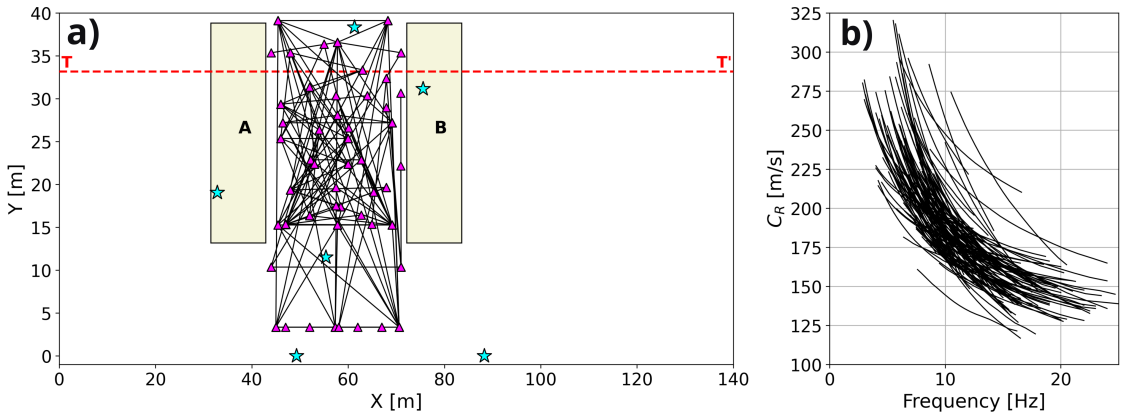


**Figure 3.2.1:** Panel (a): Schematic view of the study site. Magenta triangles depict the positions of seismic sensors, black lines connecting them show the station pairs from which dispersion curves shown in (b) were retrieved. The dashed red line represents the T-T' cross-section employed in the numerical model. Panel (b): Distribution of all Rayleigh Wave dispersion curves across the study site.

## 3.3 Retrieval of the site velocity structure

Fig. 3.3.1 displays three representative ground profile solutions, their uncertainties, and the dispersion curve fit obtained through the aforementioned procedure. Subsequently, we narrow our focus on the first 30 meters of the $V_s$ profiles, as the deeper structure is poorly resolved by the frequency range of our phase velocity data. It can be seen that the thickness of the upper layers decreases as the interstation distance decreases because the wavelengths constrained by the dispersion curves

become shorter. Additionally, the uncertainties (blue dashed line in Fig. 3.3.1) tend to increase near the depths corresponding to layer interfaces. This happens because the trade-off between layer thickness and $V_s$ cannot be resolved using only dispersion data. Nevertheless, the ground profile uncertainties are within the expected range for surface wave surveys (Vantassel and Cox, 2021, and references therein).

We used a simple merging scheme to quantify the spatial variability of $V_s$ from the ground profiles, reminiscent of the approximative tomographic inversion proposed in Kissling (1988). First, we divided the site into a rectangular grid of 35 meters in the $x$ direction and 42 meters in the $y$ direction (Fig. 3.3.2). Assuming that the surface waves travel along straight lines linking each pair of receivers, the velocity profile corresponding to each grid cell is obtained by weighting all the ground profiles corresponding to pairs of stations whose interstation path passes through it. The weighting scheme takes into account the length of each ray within the grid cell and the $\sigma_{ln,v_s}$ of each profile. In other words, the ground profile associated with the ray with the longest length within a specific grid cell carries greater weight than rays crossing shorter distances in the same grid cell. Additionally, ground profiles with lower values of $\sigma_{ln,v_s}$ for a given depth also have greater weight. Then, for a given cell that is crossed by $n$ rays of cell length $l$ and logarithmic standard deviation $\sigma^z$ at a given depth, the shear wave velocity at depth $z$, $V^z$, is given by

$$V^z = \sum_{j=1}^{n} \frac{l_j V_j^z (\sigma_j^z)^{-1}}{\sum_{k=1}^{n} l_k \sum_{k=1}^{n} (\sigma_k^z)^{-1}}, \tag{3.3.1}$$

where the subindex $s$ of the shear wave velocity term $V_s$ is omitted here for clarity. This weighting scheme ensures that rays covering more distance within a cell carry more weight, that short interstation distance models have more weight at shallow depths, and that large interstation distance models have more weight at greater depths.

Figs. 3.3.2(a)-(c) display the average velocity structure of the site at depths of 0-10 [m], 10-20 [m], and 20-30 [m]. Generally, lower velocities are observed in the shallow structure (Fig. 3.3.2a), with increasing velocities at greater depths (Figs. 3.3.2b-c).

Notably, the grid cells near the towers show relatively high velocities at all depths with respect to the middle and southernmost cells. This can be attributed to the fact that the southernmost part of the study area is located near public streets, which were likely not consolidated by heavy machinery before the building reconstruction. On the other hand, the cells in the middle are in an area that was likely consolidated and refilled before the reconstruction of the towers, but to a lesser extent than the cells adjacent to the structures. Moreover, the weight of the buildings themselves may also affect the velocity structure of the adjacent cells. Fig. 3.3.2(e) shows the weighted ground profiles for all the grids, with the black, blue, and red profiles representing cells near to, in the middle of, and to the south of the buildings, respectively. As severe liquefaction was observed near buildings A and B in 2010, the red profile (soils not consolidated by heavy machinery prior to reconstruction) is considered the most representative of the free-field natural conditions that existed for our simulations.

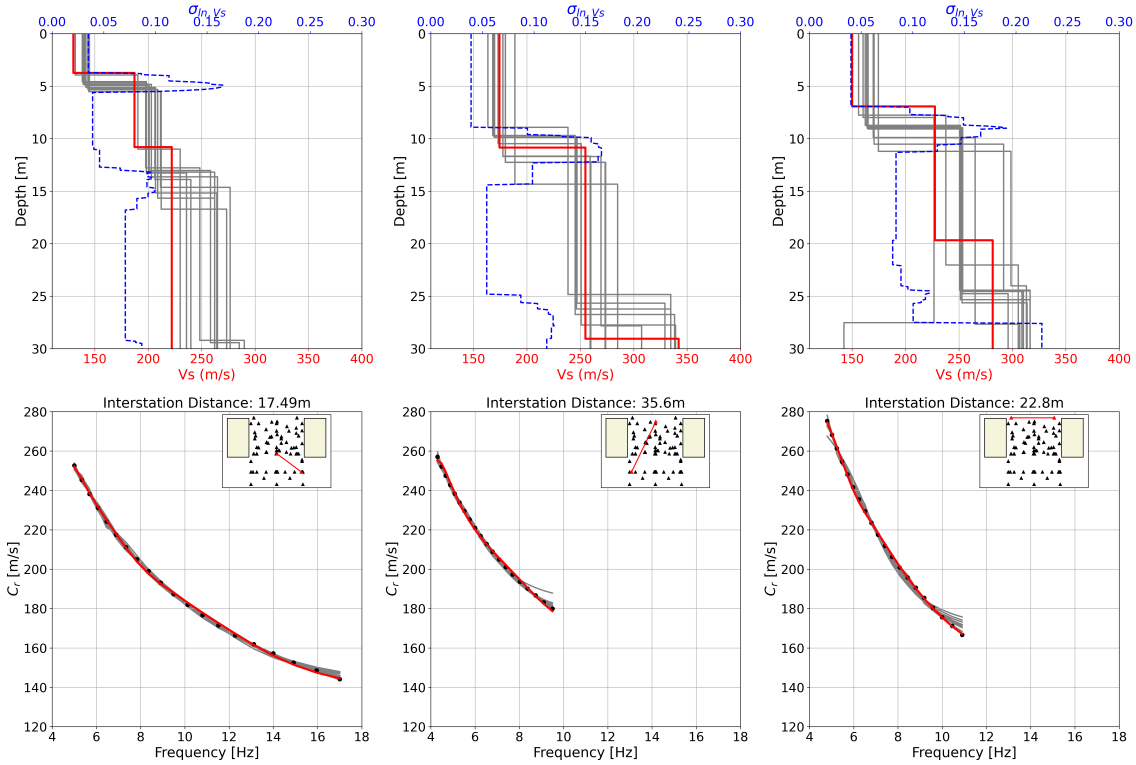


**Figure 3.3.1:** Top panels: The ground profiles inverted from the dispersion curves displayed in the lower panels. Grey profiles show the lowest misfit solution for each seed. The red profile is the lowest-misfit solution for all seeds. The dashed blue line represents the logarithm of the standard deviation of $V_s$. Lower panels: Dispersion curve fit (dotted black line) by each ground profile. Colors represent the same as at the top panels.

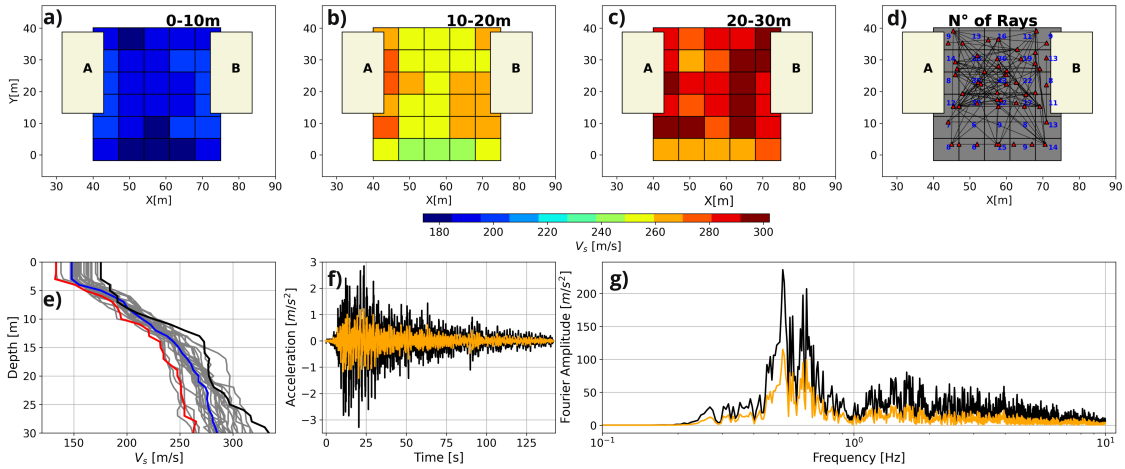


**Figure 3.3.2:** The velocity structure of the site calculated by the weighting scheme. Panels (a)-(c): Average $V_s$ structure at depths of (0-10 [m]), (10-20 [m]) and (20-30[m]), respectively. In (a)-(c), the X and Y coordinates are within the coordinate system of Fig. 3.2.1a. Panel (d): Distribution of ground profiles averaged on each grid to obtain the weighted ground profile. Panel (e): The weighted ground profiles of all grids. Three representative profiles of different ground conditions are depicted with red, blue, and black lines. The red velocity profile, which represents free-field conditions, is used for the ESSRAs. Panels (f)-(g): Black and orange ground motion and their Fourier spectrums depict the CCP EW station recording and its deconvolution to 50 meters depth, respectively.

## 3.4 Numerical Model Setup

We perform ESSRA using the Open System for Earthquake Engineering Simulation (OpenSEES) finite-element framework (McKenna, 2011) and the Scientific Toolbox for OpenSEES (Petracca et al., 2017). The wave propagation over fluid-saturated porous media is solved in a 2D domain under plane-strain conditions. We consider the cross-section T-T' depicted in Fig. 3.2.1a, a domain of 140 meters in length in the x-direction and 50 meters in depth in the z-direction, as shown in Fig. 3.4.1a. To enforce free-field conditions at the lateral boundaries of the model, we model free-field columns of 10 meters size in the x-direction and 10000 meters size in the out-of-plane direction and tie the displacement degree-of-freedom to enforce periodic boundary conditions, in a very similar manner to what is performed in Arduino and McGann (2011). The nodes at the base of the model were fixed in the z-direction, under the

assumption that the domain is underlain by an elastic homogeneous half-space, and they were forced to move horizontally in the same direction by tying them to the lower-left node. The ground motion was input at this lower-left node as a force time history using a Lysmer-Kuhlemeyer (LK) dashpot (Lysmer and Kuhlemeyer, 1969; Joyner and Chen, 1975) and propagated to the constrained base nodes and across the domain. The LK dashpot method requires to input a coefficient $c = \rho_b V_{s_b} A_{elem}$, with $\rho_b = 2.0[g/cm^3]$ and $V_{s_b} = 339[m/s]$ being the density and shear-wave velocity of the underlying medium and $A_{elem} = 10 * 10000m^2$ the basal area of the element where the ground motion is input. As neither borehole nor outcrop bedrock seismic recordings were available near our study site, the ground motion at the base was estimated by applying simple linear deamplification, to a depth of 50 meters, of the ground motion recorded at station CCP (see Fig. 3.1.1 for station location and Figs. 3.3.2(f)-(g) for the station ground motion). As mentioned earlier, our profiles are well-constrained only until a depth of 30 meters. To address this issue, we created a joint profile by taking the median of all of our non-weighted ground profiles until 30 meters, and using the profile derived for the Concepción basin from Inzunza et al. (2019) below this depth. The merged profile is shown in Table 3.4.1.

Effective stress conditions are enforced using stabilized-single-point quadrilateral $u - p$ elements (SSPQUADUP, McGann et al., 2012), which are based on the $u - p$ formulation. This formulation assumes that saturated soils are a continuum composed of a solid and a fluid phase, with the displacement of the solid phase $u$ and the pore-fluid pressure $p$ of the fluid phase being the main variables. These underlying assumptions are valid for most earthquake and soil dynamics problems (Biot, 1956; Zienkiewicz and Shiomi, 1984). SSPQUADUP elements include an additional pressure degree of freedom. As the groundwater table at the site varies from roughly 0.5 to 1.5 meters (Saldaña et al., 2023), we fixed the pore-water pressure degree-of-freedom at the surface level.

To model the elastoplastic behavior of the sands in the shallower 30 meters, we used the *PressureDependentMultiYield03* model (Khosravifar et al., 2018). This model was originally designed to capture the cyclic mobility and post-liquefaction accumulation

of shear strain on sands and has been updated to account for the influence of the number of loading cycles on liquefaction triggering. A thorough description of the model formulation can be found in Parra-Colmenares (1996); Yang et al. (2003); Khosravifar et al. (2018). We highlight from the abovementioned literature that (1) the model assumes that elastic and plastic deformations occur simultaneously in the soil, and the elastic behavior is linear and isotropic, while the plastic behavior is nonlinear and anisotropic, and (2) the soil nonlinear shear stress-strain response is defined in the octahedral space in the following manner: the pressure-dependent small-strain shear modulus $G^{p}_{max}$ is defined by

$$G^{p}_{max} = G_{max} \left( \frac{p'}{p'_r} \right)^{d}, \tag{3.4.1}$$

where $G_{max}$ is the input shear modulus computed with equation (1.0.1) at a reference effective confining stress $p'_r$, $d$ is the pressure-dependent coefficient set to 0.5, and $p'$ is the effective confining stress that varies during the earthquake loading. Thus, shear modulus reduction curves are computed using a hyperbolic relationship given by

$$\tau_{oct} = \frac{G^{p}_{max}}{1 + \frac{\gamma_{oct}}{\gamma_r} \left( \frac{p'_r}{p'} \right)^{d}} \left( \gamma_{oct} \right), \tag{3.4.2}$$

Where $\tau_{oct}$ is the octahedral shear stress, $\gamma_{oct}$ is the deviatoric strain in the octahedral space, and $\gamma_r$ is a parameter that constrains the shape of the backbone curve. Equation (3.4.2) describes the shape of the hysteretic loops for a given effective stress, small-strain shear modulus, and seismic excitation.

Most of the model input parameters apart from $G_{max}$ and the bulk modulus at a reference pressure $B_r$, which can be computed from $G_{max}$, have already been calibrated by the developers for different relative densities. Therefore, we mapped the $D_r$ values from the geostatistical model described in Saldaña et al. (2023) into our domain (Fig. 3.4.1b). Table 3.4.2 summarizes the model parameters used for our analyses. To simulate $V_s$ heterogeneity and wave attenuation, we followed the method of de la Torre et al. (2022a,b). We generated perturbations of the 1D $V_s$ profile shown in Fig. 3.3.2e, using spatially anisotropic correlated Gaussian random

fields with varying $\sigma_{ln,v_s}$ values, to simulate different levels of heterogeneity. An exponential function was used to simulate the spatial correlation, with horizontal and vertical correlation lengths set to 15 and 2 meters, respectively. Five different values of $\sigma_{ln,v_s}$ were used: 0.075, 0.125, 0.175, 0.225, and 0.275, and 20 simulations were run per level of variance, resulting in a total of 100 simulations. A zero-variance zone of 25 meters length was established at the lateral boundaries, where the 1D deterministic soil profile is valid. Fig. 3.4.1 shows the benchmark $V_s$ realization for $\sigma_{ln,v_s} = 0.075$. Lastly, a single homogeneous elastic layer of $V_s = 339\ m/s$ was used for the subdomain within 30 and 50 meters depth. The elastic half-space $V_s$ was set to 339 $m/s$. We implemented the following procedure to determine the vertical size of the elements efficiently (Ramirez et al., 2018; Tiznado et al., 2021). For small-strain problems, the maximum vertical element size, $h_{max}$, depends on the $V_s$ value of the element and the maximum frequency of the input motion: $h_{max} = \frac{V_s}{4f_{max}}$. As the shear modulus degrades in nonlinear problems, this implies that $V_s$ will decrease as the simulations progress. Therefore, to ensure that our elements do not exceed their theoretical maximum size we further divided $h_{max}$ by a factor of 4 to account for this phenomenon and guarantee that a sufficient number of elements cover one wavelength at all times.

The numerical analysis consists of three stages. In the first stage, a gravity analysis is conducted to apply self-weight to the model and initialize the stress state over the soil domain before applying the seismic load. At this point, the soil behavior is considered as linear elastic in the whole domain. In the second stage, a second gravity analysis is conducted but now the elastoplastic behavior of the soil materials is enforced in the shallower 30 meters of the domain, while the deepest part of the domain behaviors remains as linear elastic. In the third stage, the earthquake load is applied at the base of the domain. We used the Penalty Method to constrain the equations in the analysis, the MUltifrontal Massively Parallel sparse direct Solver (MUMPS) solver (Amestoy et al., 2000) to solve the system of equations, a Krylov-Newton algorithm to determine the sequence of steps to solve the non-linear equation (Scott and Fenves, 2010), and the Newmark integrator (Newmark, 1959) to solve the differential equations with $\gamma = 0.5$ and $\beta = 0.25$. Finally, we used an adaptive time

step to increase the accuracy, stability, and efficiency of the solution.

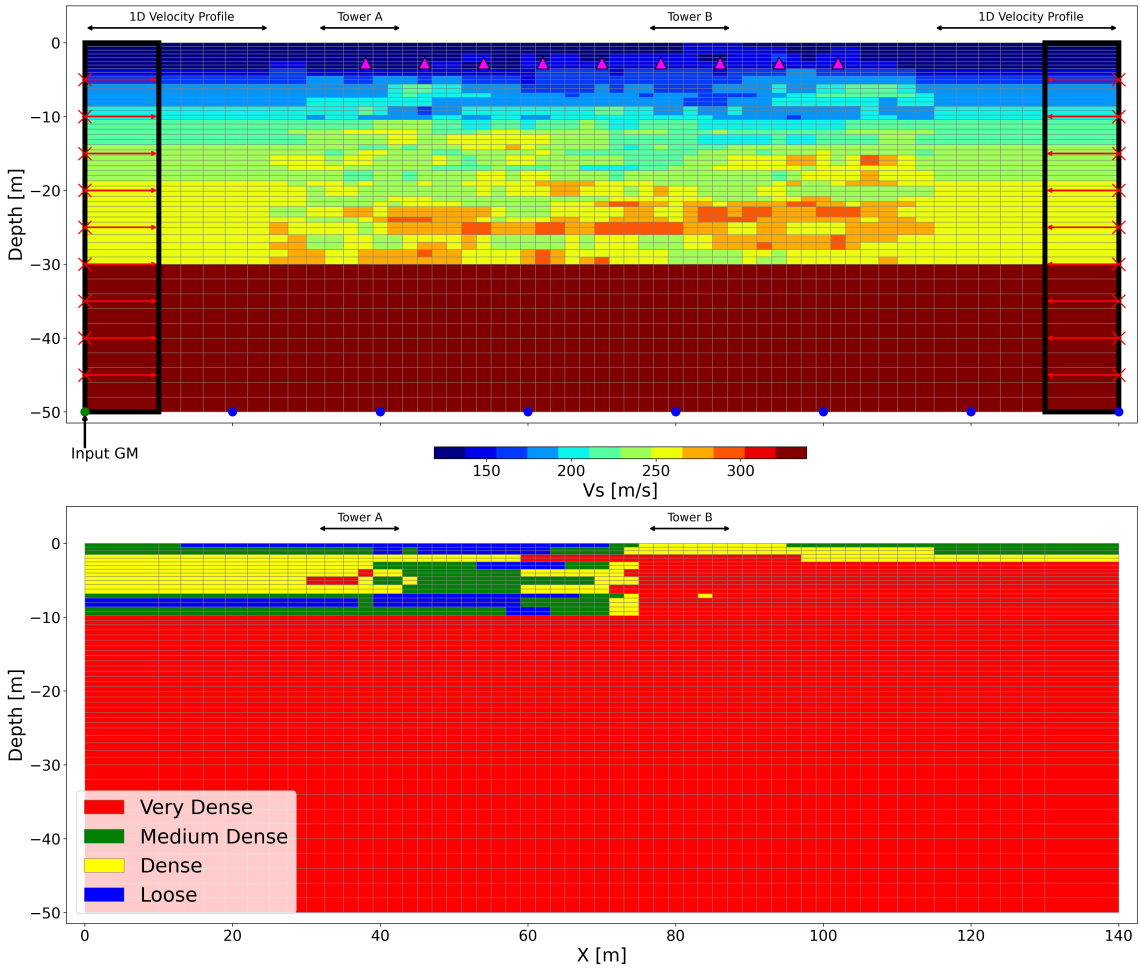


**Figure 3.4.1:** Benchmark finite element model realization of the T-T' cross-section defined in Fig. 3.2.1. Top panel: $V_s$ random field obtained using $\sigma_{ln,v_s} = 0.075$. Free-field columns at the lateral boundaries are depicted in thick black rectangles. The red arrows start and end at the main and constraint nodes, respectively. Input ground motion is applied at the green node in the lower-left corner. Base nodes (blue) are constrained to the green node. The recorder nodes at a depth of three meters are depicted as magenta triangles and are further analyzed in Fig.4.2.1. Lower panel: $D_r$ structure of the cross-section (Saldaña et al., 2023).

| Layer | Thickness $[m]$ | $V_s[m/s]$ | $\rho[g/cm^3]$ | Source |
|---|---|---|---|---|
| 1 | 4 | 131 | 1.9 | This work |
| 2 | 7 | 198 | 1.9 | This work |
| 3 | 17 | 255 | 1.9 | This work |
| 4 | 22 | 339 | 1.9 | Inzunza et al. (2019) |
| 5 | $\infty$ | 339 | 2.0 | Inzunza et al. (2019) |

**Table 3.4.1:** Joint ground profile obtained by merging the median profile from this work and the uppermost two layers of the profile derived in Inzunza et al. (2019).

| Model parameters | Loose sand | Medium dense sand | Dense sand | Very dense sand |
|---|---|---|---|---|
| Relative density ($D_r$) | 33% | 57% | 74% | 87% |
| Mass density $\rho$ $[g/cm^3]$ | 1.9 | 1.9 | 1.9 | 1.9 |
| Ref. Shear Modulus $G_{max,r}$ | from $V_s$ | from $V_s$ | from $V_s$ | from $V_s$ |
| Ref. Bulk Modulus $B_r$ | from $V_s$ | from $V_s$ | from $V_s$ | from $V_s$ |
| Model friction angle | 25.4 | 30.3 | 35.8 | 42.2 |
| Peak shear strain | 0.1 | 0.1 | 0.1 | 0.1 |
| Ref. mean eff. press. | Depth depend. | Depth Depend. | Depth Depend. | Depth Depend. |
| Press. dependence coeff., $d$ | 0.5 | 0.5 | 0.5 | 0.5 |
| Phase transf. angle [°] | 20.4 | 25.3 | 30.8 | 37.2 |
| Contraction coeff. $c_a$ | 0.03 | 0.012 | 0.005 | 0.001 |
| Contraction coeff. $c_b$ | 5.0 | 3.0 | 1.0 | 0.0 |
| Contraction coeff. $c_c$ | 0.2 | 0.4 | 0.6 | 0.8 |
| Contraction coeff. $c_d$ | 0.0 | 0.0 | 0.0 | 0.0 |
| Contraction coeff. $c_e$ | 0.0 | 0.0 | 0.0 | 0.0 |
| Dilation coeff. $d_a$ | 0.15 | 0.3 | 0.45 | 0.6 |
| Dilation coeff. $d_b$ | 3.0 | 3.0 | 3.0 | 3.0 |
| Dilation coeff. $d_c$ | -0.2 | -0.3 | -0.4 | -0.5 |
| Permeability coeff. | from $I_c$ | from $I_c$ | from $I_c$ | from $I_c$ |
| Number of yield surfaces | 20 | 20 | 20 | 20 |

**Table 3.4.2:** PressureDependentMultiYield03 model parameters employed in this research.

# Chapter 4

# Results

In the Results and Discussion sections, we describe and analyze the simulation results from five measurements:

- The shear strain $\gamma$.
- The volumetric strain $\epsilon_v$, defined as the mean of the vertical and horizontal strains.
- The excess pore-water pressure ratio $r_u$, defined as the difference between the current and initial pore-water pressure divided by the overburden effective stress.
- The vertical settlements $u_z$.
- The horizontal acceleration $a_x$

Threshold values previously defined in the literature for liquefaction triggering are between 80% and 100% for $r_u$, and between 3% and 5% for the shear strains (Ishihara, 1993; Boulanger et al., 1998; Bray and Sancio, 2006).

## 4.1 Benchmark Simulation

Fig. 4.1.1 shows the maximum $\gamma$, maximum $\epsilon_v$, maximum $r_u$, maximum horizontal acceleration $a_x$, and final vertical settlement $u_z$ for the benchmark model realization shown in Fig. 3.4.1. We focus on three representative nodes, which are depicted as white circles 1, 2, and 3 in Fig. 4.1.1. For the zone surrounding representative node 1, liquefaction of a loose sand layer (see Fig. 3.4.1b) occurs at depths between 7-8 meters as evidenced by the accumulation of large strains (Fig. 4.1.1a-b) and $r_u$ values exceeding 100% being located in this part (Fig. 4.1.1c). The highly nonlinear hysteretic loops of the stress-strain curve and the $r_u$ time series are also consistent with liquefaction phenomena (Fig. 4.1.2a). Moreover, a steep gradient of horizontal accelerations is observed below the node (Fig. 4.1.1d).

For the zone surrounding representative node 2, we observe slightly smaller maximum $r_u$ values ($\sim 90-100\%$, Fig. 4.1.1c) and maximum shear strains in the range of $2-4\%$ (Fig. 4.1.1a). These $r_u$ and shear strain values are close to the previously stated threshold values. The stress-strain response recorded is nonlinear (Fig. 4.1.2b), but to a considerably lesser extent than node 1. Furthermore, the maximum volumetric strains are negative (indicating contraction) near node 2, but the surface values are positive (indicating dilation) (Fig. 4.1.1a). The area around node 2 is the one that exhibits the largest vertical settlements, reaching roughly 50 millimeters (Fig. 4.1.1e).

As for the zone surrounding representative node 3, no liquefaction occurs. Indeed, $r_u$ values do not exceed 50% (Fig. 4.1.1c), the stress-strain behavior is close to linear (Fig. 4.1.2c), no significant settlements are observed (Fig. 4.1.1e), and the maximum accelerations are significantly higher than in the zone around node 2 (Fig. 4.1.1d), implying that this zone did not experience significant soil softening. As shown in Fig. 3.4.1b, node 3 is embedded in a zone of dense sands, which are less susceptible to liquefaction compared to the layers in which nodes 1 and 2 are situated.

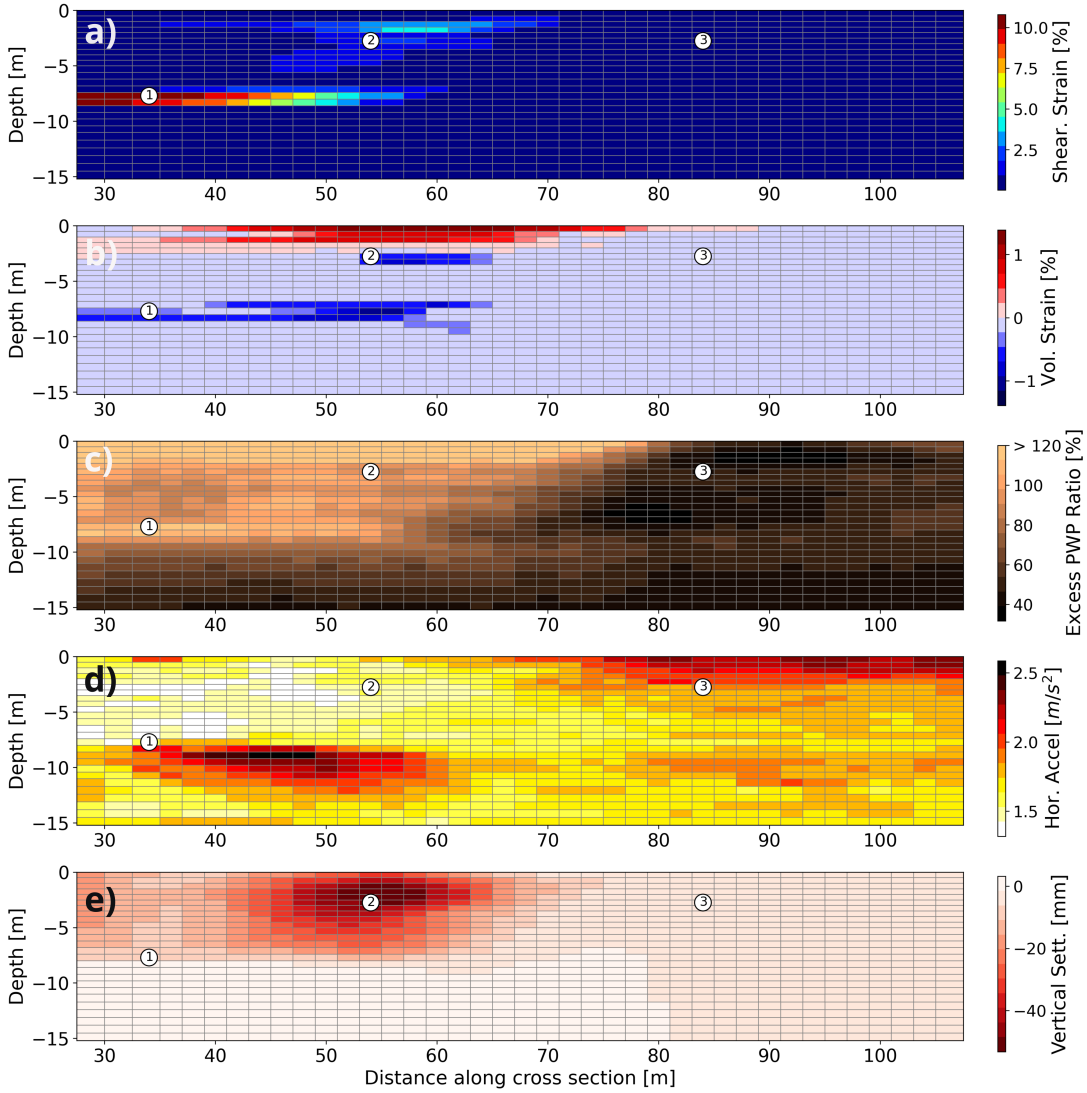


**Figure 4.1.1:** Maximum shear strain (a), volumetric strain (b), excess pore-water pressure ratio (c), horizontal acceleration (d), and settlements (e) for the benchmark model realization shown in Fig. 3.4.1. The magenta numbered circles represent the locations of the three nodes depicted in Fig. 4.1.2.

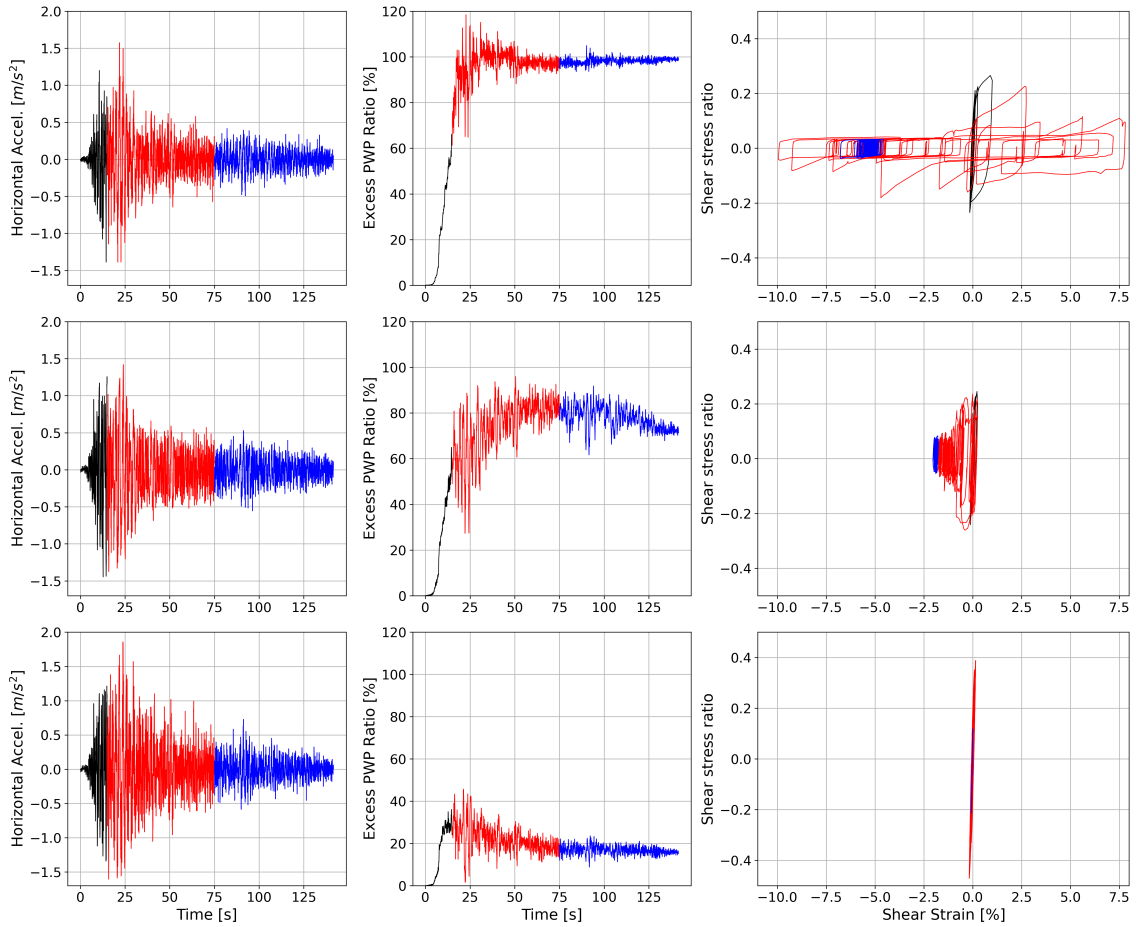


**Figure 4.1.2:** Recorder acceleration, excess pore-water pressure, and stress-strain time series of the numbered nodes of Fig. 4.1.1. Top panel: Node 1. Middle panel: Node 2. Bottom panel: Node 3. The time series' black, red, and blue color codes represent the first 15 seconds of motion, from 15 to 75 seconds, and from 75 to the end of motion.

## 4.2 Assessing the effect of $V_s$ variability on key dynamic properties

In Fig. 4.2.1, we plot, for different levels of $\sigma_{ln,v_s}$, the median maximum $\gamma$, $\epsilon_v$, $r_u$, and $u_z$ of all simulations as a function of the distance along the cross-section at a depth of 2 meters. The cross-section's nine nodes — five positioned to the west and four to the east — display distinct behaviors. Consequently, we conduct separate

analyses for the two cases. For the western nodes, the high $r_u$ $(80-100\%)$ values for all $\sigma_{ln,v_s}$ levels are indicative of liquefaction behavior. Particularly, we can see that an increase in $\sigma_{ln,v_s}$ leads to a decrease in the median maximum $\gamma$ and $\epsilon_v$. In a similar manner, a slight reduction in the median maximum $u_z$ is observed at the nodes $x = 46[m]$ and $x = 54[m]$ as $\sigma_{ln,v_s}$ drops. This tendency is not observed for the rest of the western nodes, and the median maximum $u_z$ values are very similar. Additionally, no significant changes in the median maximum $r_u$ values are observed.

For the eastern nodes, the low $r_u$ $(45-50\%)$ values and the developed small strains and settlements indicate that no liquefaction occurred. Furthermore, we appreciate very slight variabilities in the soil response for different levels of $\sigma_{ln,v_s}$. Only a slight increase in the median maximum $r_u$ values with increasing $\sigma_{ln,v_s}$ is observed, which is a contrary behavior to what is seen in western nodes. Anyhow, variations on $\sigma_{ln,v_s}$ did not signify a change in the eastern nodes from non-liquefaction to liquefaction behavior. Although the values are slightly different, a very similar behavior for the western and eastern nodes is observed at depths of 4 and 5 meters (Figs. S2.1-S2.2).

Fig. 4.2.2 shows the time series of the aforementioned variables for all the simulations (grey lines) and the median time series at different levels of $\sigma_{ln,v_s}$ for the western node $x = 54[m]$ (see Fig. 4.2.1 for node location). This is the node that exhibited the largest median maximum shear strain and settlements. Overall, we see that all the median time series closely follow each other in the first 20 seconds, when $r_u$ values are not large. After the 20 seconds, and even more markedly at around 45 seconds (i.e., when $r_u$ stabilizes and stops increasing), differences between the $\sigma_{ln,v_s}$ levels become apparent. In the same line, we see that all simulations (regardless of $\sigma_{ln,v_s}$) follow the pattern of permanent strain accumulation when high pore-water pressures are developing. This implies that liquefaction behavior occurs regardless of the simulation $\sigma_{ln,v_s}$ level. Additionally, the same tendency of greater $\sigma_{ln,v_s}$ leading to smaller strains and settlements observed in Fig. 4.2.1 is noted for the median time series. It can be appreciated as well that starting from $t > 40s$, the higher median $r_u$ values happen for $\sigma_{ln,v_s} = 0.075$, but the increase is slight.

Black curves in Fig. 4.2.2 show all model simulations' 20-th and 80-th percentiles. For the strains and $r_u$ time series, $\sigma_{ln,v_s} = 0.075$ and $\sigma_{ln,v_s} = 0.275$ curves follow closely the 80-th and 20-th percentile curves, respectively. On the other hand, we see from the vertical displacement time series that the percentile curves are farther off from the median curves than for the strain and $r_u$ time series. Actually, the settlement $u_z$ (i.e., the last value of the time series) for the 20-th and 80-th percentiles considerably varies from 41 to 53 millimeters. We can also see that the volumetric and vertical displacements are still increasing at the last time step. This could indicate that flow is still occurring after the strong motion has ended, and hence larger settlements could be obtained by increasing the simulation time. A similar pattern is observed for the time series at depths of 4 and 5 meters (Figs. S2.3-S2.4).

For comparison, we also show the time series for the eastern node $x = 86[m]$ Fig. 4.2.3. From here, we mention two noteworthy points: The first is that shear strain, pore-water pressure ratio, and vertical displacement median time series for each $\sigma_{ln,v_s}$ are much more stacked together than in the previous case. Additionally, we appreciate more variability in the volumetric strains, although the maximum magnitude of the strains accumulated is smaller than 0.05. With that in mind, even though the 20-th and 80-th of volumetric strains and vertical displacements are farther off from the median curves, their values are very small. The second is that no liquefaction behavior is observed even for the most extreme outliers simulations (i.e., the ones that exhibit the largest $r_u$). This is in agreement with what we had shown for the eastern nodes in Fig. 4.2.1.

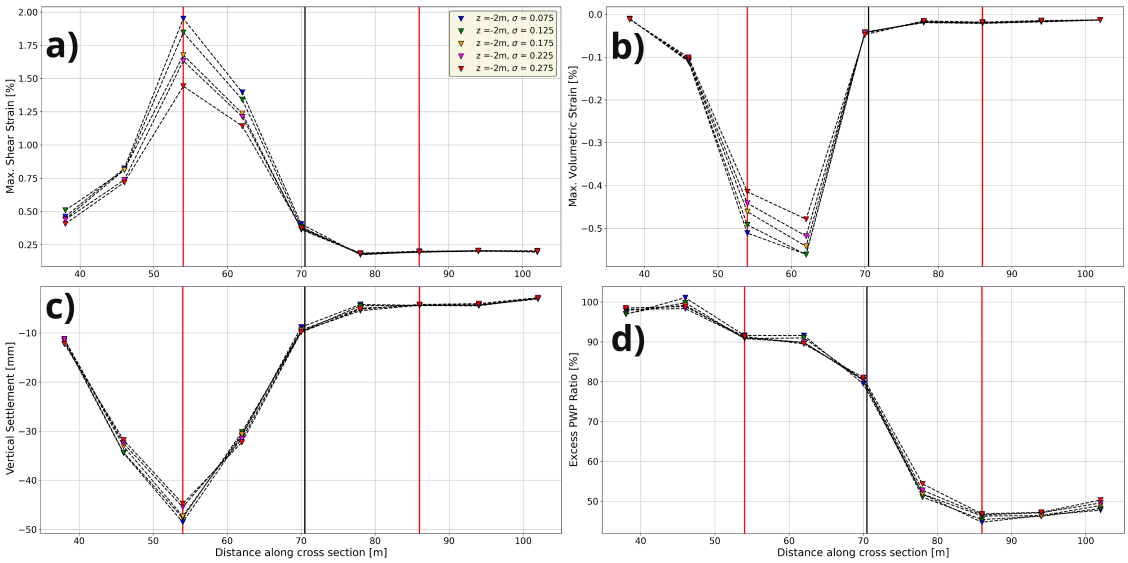


**Figure 4.2.1:** Median of the max. shear strain (a); max. volumetric strain (b); max. PWP ratio (c); and vertical settlements (d); at different levels of $\sigma_{ln,v_s}$ across the T-T' cross-section. Nodes are located at a depth of 2 meters. Thick black vertical line divides the western from eastern nodes. Thick red vertical lines depict the location of the western and eastern nodes analyzed in Figs. 4.2.2 and Fig. S2.5. Horizontal black lines near the x-axis represent the locations of towers A and B relative to the cross-section.

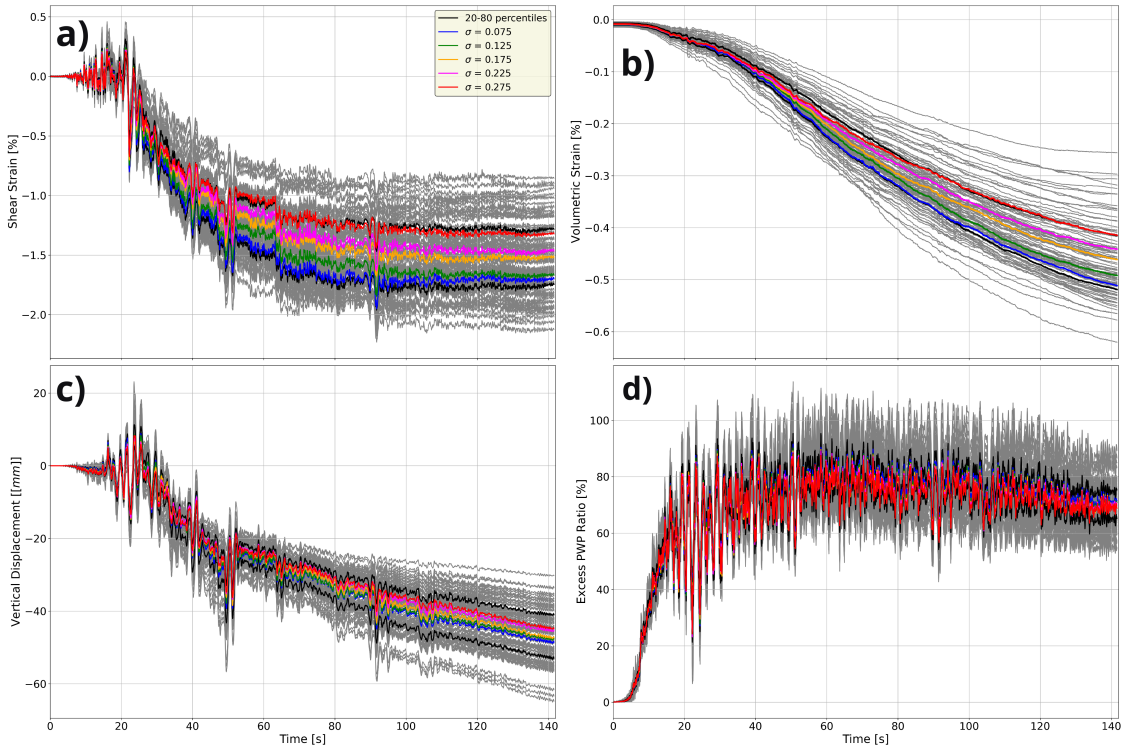


**Figure 4.2.2:** All simulations of shear strain (a), volumetric strain (b), vertical displacement (c), and excess pore-water pressure ratio (d) time series computed for the node at the western node at position $x = 54$ and depth of 2 meters, depicted in Fig. 4.2.1. Color-coded time series represent the median time series at different levels of $\sigma_{ln,v_s}$. Black curves represent all simulations' 20-th and 80-th percentile time series.

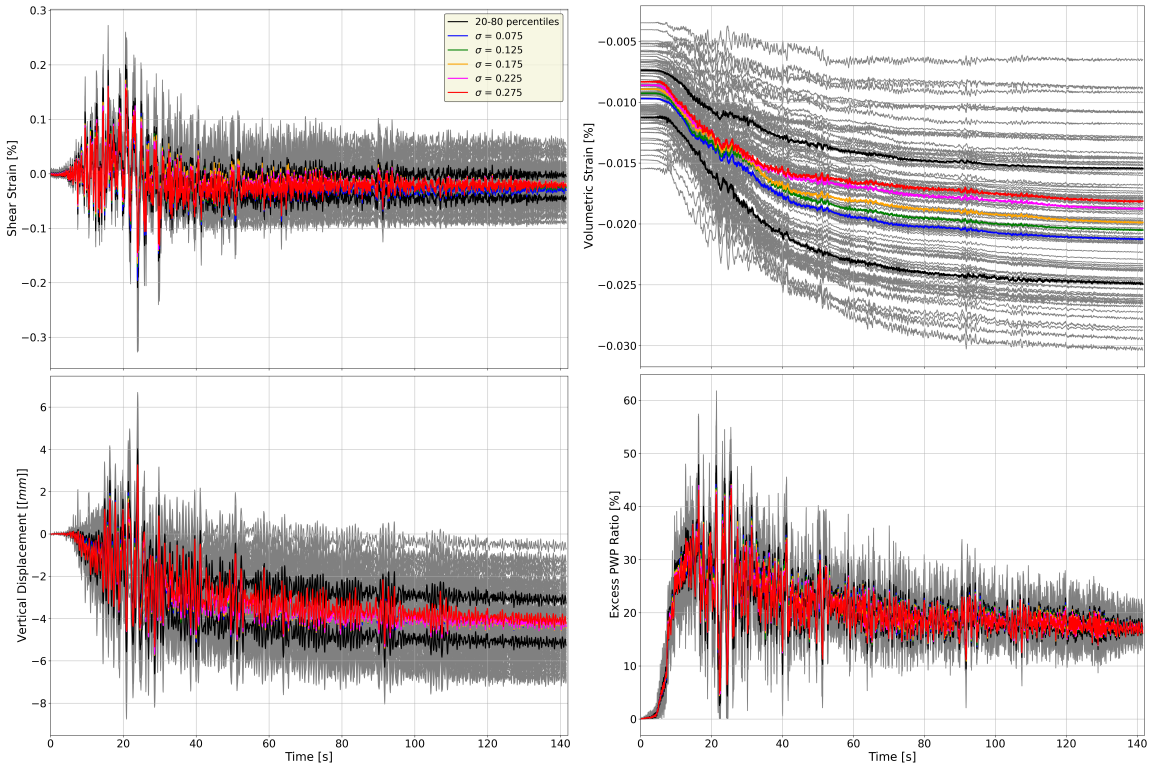


**Figure 4.2.3:** The same parameters, represented in the same colors, as for Fig. 4.2.2, but this time for the eastern node at position $x = 86$ and depth of 2 meters.

# Chapter 5

# Discussion

Our findings indicate distinct responses between western and eastern nodes due to the varying levels of $V_s$ spatial variability. While strains and settlements tend to decrease as variability increases for the western nodes, the response of the eastern nodes remains relatively unchanged. In Fig. 4.2.2, we see that the western node was subjected to large plastic deformations across all $\sigma_{ln,v_s}$ levels, while Fig. S2.5 demonstrates minimal deformations for all simulations at the eastern node. From this, and recalling from Fig. 3.4.1 that the shallow western part of the domain corresponds to soil units with low relative density, and the shallow eastern part of the domain corresponds to units with high relative density, it can be inferred that $V_s$ spatial variability may not alter the soil's intrinsic response to liquefaction. This response is likely primarily controlled by the soil's mechanical properties and the earthquake loading. In other words, our results support the notion that $V_s$ spatial variability does not play a primary role in liquefaction triggering, but rather influences the liquefaction response when liquefaction is already ongoing.

We propose a physical explanation for the decrease in liquefaction-induced settlements and strains as $\sigma_{ln,v_s}$ increases. As seen in Fig. 4.2.2a, the median curves diverge as nonlinear behavior increases (i.e., plastic deformation develops during the simulation). We can infer that the more nonlinear the behavior of the soil is, the increased

importance of $\sigma_{ln,v_s}$ becomes apparent. Certainly, it is known that for a given shear-wave velocity value, the soil damping increases with larger shear strains (Hashash and Park, 2001, 2002). Therefore, if variability increases, the overall soil stiffness decreases, intensifying the damping and reproducing the observed deformation patterns. It should be noted that this pattern depends on the median $V_s$ values of the soil units. If $V_s$ is high, the damping will be lower due to the increased shear strength of the soil, reducing the importance of $\sigma_{ln,v_s}$. See, for instance, Fig. S6, which displays the shear-strain time series of node number 1 from Fig. 4.1.1, where significant liquefaction was observed between 7 and 8 meters depth. Even though larger shear strains close to 10% are appreciated, the median time series do not exhibit a clear relationship between $\sigma_{ln,v_s}$ and the developed shear strains. In summary, we propose that the influence of $\sigma_{ln,v_s}$ on the liquefaction response becomes relevant in the following circumstances:

1. The ground motion intensity is strong enough to trigger nonlinear behavior and significant $r_u$ values.

2. The mechanical properties of the soil allow liquefaction to occur.

3. The median $V_s$ of the soil at a given depth is sufficient to allow significant damping when subjected to large (e.g., $> 1\%$) shear strains for a given ground motion intensity.

In terms of liquefaction-induced settlements, one of the most detrimental liquefaction hazards, our results show that the effect of $V_s$ spatial variability on the median computed settlements was consistent but slight. However, the settlements' 20-th and 80-th percentiles are 41 and 53 millimeters, respectively. This implies that $V_s$ variability may significantly influence the computed settlements. Therefore, it is crucial to constrain the velocity structure of a site accurately in order to gain a better insight into the liquefaction response of a case study. With this in mind, we identified three distinct $V_s$ profiles consistent with the site's geophysical and geotechnical characteristics within our small study site. For bigger soil domains (e.g.,

Pretell et al., 2021; Qiu et al., 2023), we can expect to see even more diverse $V_s$ signatures.

We note that the calculated maximum shear strains near the surface are not larger than 3%, which is not considered to be exceedingly large. Saldaña et al. (2023) conducted ESSRAs at the same study site and obtained maximum surface shear strains near the surface up to 10%. Additionally, simulations of Luque and Bray (2017) on two buildings - that exhibited liquefaction-induced settlements during the Canterbury Earthquake Sequence of 2010-2011 - reached maximum shear strains beneath the buildings of around 8%. We suggest that the effect of $V_s$ heterogeneities on near-surface deformations may be more significant in these cases compared to our study.

While it was not our primary research goal, we compared the computed settlements at the representative nodes of Towers A and B in Tables 5.0.1 and 5.0.2, respectively. Our average settlements of 1.14 cm for Tower A and 0.47 cm for Tower B are significantly lower than the LiDAR measured values of 18.47cm and 9.02 cm. However, we were able to replicate the general tendency of larger settlements at Tower A compared to Tower B. Saldaña et al. (2023) obtained a good agreement between data and predicted settlements at Tower A and Tower B using a very similar geotechnical characterization and model formulation, but modeled the buildings as uniform loads. We argue that it is likely that our worse prediction of the observations may be attributed to performing the simulations in free-field conditions.

| | $\sigma = 0.075$ | $\sigma = 0.125$ | $\sigma = 0.175$ | $\sigma = 0.225$ | $\sigma = 0.275$ | LiDAR |
|---|---|---|---|---|---|---|
| minimum | 1.05 | 0.91 | 0.894 | 0.76 | 0.71 | 6.94 |
| average | 1.16 | 1.12 | 1.12 | 1.16 | 1.16 | 18.47 |
| maximum | 1.33 | 1.31 | 1.49 | 1.54 | 1.57 | 34.5 |

**Table 5.0.1:** Minimum, average, and maximum settlements (in centimeters) obtained at tower A (node $x = 38$) for different levels of $V_s$ spatial variability.

| | $\sigma = 0.075$ | $\sigma = 0.125$ | $\sigma = 0.175$ | $\sigma = 0.225$ | $\sigma = 0.275$ | LiDAR |
|---|---|---|---|---|---|---|
| minimum | 0.32 | 0.27 | 0.24 | 0.19 | 0.14 | 7.6 |
| average | 0.43 | 0.45 | 0.48 | 0.49 | 0.49 | 9.02 |
| maximum | 0.57 | 0.57 | 0.66 | 0.73 | 0.79 | 10.7 |

**Table 5.0.2:** Minimum, average, and maximum settlements (in centimeters) obtained at tower B (node $x = 78$) for different levels of $V_s$ spatial variability.

## 5.1 Further Work

Our case study represents the site response modeling of a relatively small area that exhibited liquefaction-induced damage in the context of a megathrust long-duration earthquake with moderate peak-ground accelerations. While our results clearly show a relationship between the $V_s$ spatial variability and the computed strains and settlements, our research provides support for future work that could extend and complement our results. For example, the influence of ground motion variability could be assessed by using a methodology such as the one shown in (Pretell et al., 2019, 2021). In their research, they assume that the behavior of the soil is linear, rotate the horizontal components of a near recording (e.g., our CCP recording), and the component parallel to their site of study is used to generate a suite of 20 equally possible input ground motion realizations. Also, it would be interesting to perform similar studies on sites with a greater spatial extent, and that are within a different tectonic environment. The Northridge Earthquake of 1994 ($M_w$ 6.7) and the Christchurch Earthquake of 2011 ($M_w$ 6.1) were shallow earthquakes that released much less seismic moment than the Maule earthquake, but due to the proximity of the events to urban areas, widespread liquefaction damages were reported (Holzer et al., 1999; Green et al., 2014; Pretell et al., 2021). Finally, 3D site response analyses could be performed in order to obtain a more general conclusion about the effects of $V_s$ spatial variability in soil response, but we note that the computational cost of running several 3D model realizations is very expensive.

# Chapter 6

# Conclusion

We performed effective stress analyses (ESSRAs) at the Los Presidentes site, which experienced liquefaction damage during the 2010 $M_w$ 8.8 Maule Earthquake, in order to assess the effects of $V_s$ heterogeneities on liquefaction response at the site. Using seismic interferometry methods, we identified three distinct velocity profiles representative of the site conditions. Using the profile that most accurately represented free-field conditions, we generated 2D $V_s$ heterogeneous model realizations at various levels of $\sigma_{ln,v_s}$ using Gaussian correlated random fields. Our simulation results demonstrate that increasing $\sigma_{ln,v_s}$ in near-surface soil elements, which exhibit nonlinear and liquefaction-like behavior due to earthquake-induced pore-water pressure buildup, leads to a decrease in median maximum shear, volumetric strains, and vertical settlements. We argue that when nonlinear behavior begins, an increase in damping at the element level is responsible for this reduction in the computed measurements. Furthermore, the influence of $\sigma_{ln,v_s}$ on the liquefaction response is more pronounced at shallow depths, where both $V_s$ values and the confining pressure values are lower because the damping of the soil is stiffness-dependent. On the other hand, increasing $\sigma_{ln,v_s}$ did not significantly alter the deformation patterns of soil elements that exhibit non-liquefaction behavior. This implies that $V_s$ influence on liquefaction triggering is minimal and that the soil's mechanical properties and the intensity of the seismic

motion are the primary factors in determining whether liquefaction is triggered or not.

In the frame of liquefaction hazard assessment, the maximum computed settlements at the 20-th and 80-th percentiles were 41 and 53 millimeters, respectively. This highlights a significant difference considering that our simulations were conducted without accounting for the building's load, and that the computed maximum shear strains were relatively small ($< 3\%$). We infer that for higher amplitude ground motions and softer soil conditions, $V_s$ variability may play an important role in the final settlements and deformations because the nonlinear behavior of the soil will be accentuated.

While our findings are within the frame of a case study of liquefaction due to a megathrust earthquake, this analysis can be extended to other tectonic and geotechnical environments. In this regard, we encourage researchers to thoroughly characterize the velocity structure of a site when conducting ESSRAs for past or expected liquefaction case studies as $V_s$ heterogeneities, which are expected to be found in the scale of liquefaction problems, can significantly alter the dynamic response of liquefiable soils, and become a key factor for liquefaction hazard assessment.

# Bibliography

Aki, K. (1957). Space and Time Spectra of Stationary Stochastic Waves, with Special Reference to Microtremors. *Bulletin of the Earthquake Research Institute*, 35:415–456.

Aki, K. (1980). Attenuation of shear-waves in the lithosphere for frequencies from 0.05 to 25 Hz. *Physics of the Earth and Planetary Interiors*, 21(1):50–60.

Alessio, G., Alfonsi, C., Brunori, P., Burrato, G., Casula, G., et al. (2013). Liquefaction phenomena associated with the Emilia earthquake sequence of May–June 2012 (Northern Italy). *Natural Hazards and Earth System Sciences*, 13(4):935–947.

Amestoy, P. R., Duff, I. S., L'Excellent, J.-Y., and Koster, J. (2000). Mumps: a general purpose distributed memory sparse solver. In *International Workshop on Applied Parallel Computing*, pages 121–130. Springer.

Andrus, R. D. and Stokoe II, K. H. (2000). Liquefaction Resistance of Soils from Shear-Wave Velocity. *Journal of Geotechnical and Geoenvironmental Engineering*, 126(11):1015–1025.

Arduino and McGann (2011). Dynamic 2D Effective Stress Analysis of Slope. https://opensees.berkeley.edu/wiki/index.php/Dynamic_2D_Effective_Stress_Analysis_of_Slope. Last checked on December, 2023.

Assimaki, D. (2004). *Topography effects in the 1999 Athens earthquake: Engineering issues in seismology*. PhD thesis, Massachusetts Institute of Technology.

Assimaki, D., Ledezma, C., Montalva, G. A., Tassara, A., Mylonakis, G., and Boroschek, R. (2012). Site Effects and Damage Patterns. *Earthquake Spectra*, 28(1_suppl1):55–74.

Assimaki, D., Pecker, A., Popescu, R., and Prevost, J. (2003). Effects of spatial variability of soil properties on surface ground motion. *Journal of Earthquake Engineering*, 7(spec01):1–44.

Asten, M. W. and Henstridge, J. (1984). Array estimators and the use of microseisms for reconnaissance of sedimentary basins. *Geophysics*, 49(11):1828–1837.

Baser, T., Nawaz, K., Chung, A., Faysal, S., and Numanoglu, O. A. (2023). Ground movement patterns and shallow foundation performance in Iskenderun coastline during the 2023 Kahramanmaras earthquake sequence. *Earthquake Engineering and Engineering Vibration*, pages 1–15.

Bassal, P. C. and Boulanger, R. W. (2021). System Response of an interlayered Deposit with Spatially Preferential Liquefaction Manifestations. *Journal of Geotechnical and Geoenvironmental Engineering*, 147(12):05021013.

Bassal, P. C. and Boulanger, R. W. (2023). System response of an interlayered deposit with a localized graben deformation in the Northridge earthquake. *Soil Dynamics and Earthquake Engineering*, 165:107668.

Bensen, G., Ritzwoller, M., Barmin, M., Levshin, A. L., Lin, F., Moschetti, M., Shapiro, N., and Yang, Y. (2007). Processing seismic ambient noise data to obtain reliable broad-band surface wave dispersion measurements. *Geophysical Journal International*, 169(3):1239–1260.

Biot, M. A. (1956). Theory of Propagation of Elastic Waves in a Fluid-Saturated Porous Solid. II. Higher Frequency Range. *The Journal of the Acoustical Society of America*, 28(2):179–191.

Bonnefoy-Claudet, S., Cotton, F., and Bard, P.-Y. (2006). The nature of noise wavefield and its applications for site effects studies: A literature review. *Earth-Science Reviews*, 79(3-4):205–227.

Boulanger, R. W. and Idriss, I. (2014). CPT and SPT based liquefaction triggering procedures. *Report No. UCD/CGM.-14*, 1.

Boulanger, R. W., Meyers, M. W., Mejia, L. H., and Idriss, I. M. (1998). Behavior of a fine-grained soil during the Loma Prieta earthquake. *Canadian Geotechnical Journal*, 35(1):146–158.

Boulanger, R. W. and Montgomery, J. (2016). Nonlinear deformation analyses of an embankment dam on a spatially variable liquefiable deposit. *Soil Dynamics and Earthquake Engineering*, 91:222–233.

Bray, J., Arduino, P., Ashford, S., Asimaki, D., Eldridge, T., Frost, J., Hashash, Y., Hutchinson, T., Johnson, L., Kelson, K., Kayen, R., Ledezma, C., Moss, R., Mylonakis, G., Olson, S., Rollins, K., Sitar, N., Stewart, J., Urzua, A., and Zoa, N. (2010). Geo-Engineering Reconnaissance of the 2010 Maule, Chile Earthquake. pages 1–347.

Bray, J., Rollins, K., Hutchinson, T., Verdugo, R., Ledezma, C., Mylonakis, G., Assimaki, D., Montalva, G., Arduino, P., Olson, S. M., et al. (2012). Effects of ground failure on buildings, ports, and industrial facilities. *Earthquake Spectra*, 28(1_suppl1):97–118.

Bray, J. D. and Luque, R. (2017). Seismic performance of a building affected by moderate liquefaction during the Christchurch earthquake. *Soil Dynamics and Earthquake Engineering*, 102:99–111.

Bray, J. D. and Sancio, R. B. (2006). Assessment of the liquefaction susceptibility of fine-grained soils. *Journal of Geotechnical and Geoenvironmental engineering*, 132(9):1165–1177.

Campos, J., Hatzfeld, D., Madariaga, R., López, G., Kausel, E., Zollo, A., Iannacone, G., Fromm, R., Barrientos, S., and Lyon-Caen, H. (2002). A seismological study of the 1835 seismic gap in south-central Chile. *Physics of the Earth and Planetary Interiors*, 132(1-3):177–195.

Chávez-García, F. J., Rodríguez, M., and Stephenson, W. R. (2005). An alternative approach to the SPAC analysis of microtremors: exploiting stationarity of noise. *Bulletin of the Seismological Society of America*, 95(1):277–293.

Cox, B. R. and Teague, D. P. (2016). Layering ratios: a systematic approach to the inversion of surface wave data in the absence of a priori information. *Geophysical Journal International*, 207(1):422–438.

Cubrinovski, M., Rhodes, A., Ntritsos, N., and Van Ballegooy, S. (2019). System response of liquefiable deposits. *Soil Dynamics and Earthquake Engineering*, 124:212–229.

Curtis, A., Gerstoft, P., Sato, H., Snieder, R., and Wapenaar, K. (2006). Seismic interferometry—Turning noise into signal. *The Leading Edge*, 25(9):1082–1092.

Dashti, S. and Bray, J. D. (2013). Numerical simulation of building response on liquefiable sand. *Journal of Geotechnical and Geoenvironmental Engineering*, 139(8):1235–1249.

de la Torre, C. A., Bradley, B. A., and McGann, C. R. (2022a). 2d Geotechnical site-response analysis including soil heterogeneity and wave scattering. *Earthquake Spectra*, 38(2):1124–1147.

de la Torre, C. A., Bradley, B. A., Stewart, J. P., and McGann, C. R. (2022b). Can modeling soil heterogeneity in 2D site response analyses improve predictions at vertical array sites? *Earthquake Spectra*, page 87552930221105107.

Díaz, J., Ruiz, M., Sánchez-Pastor, P. S., and Romero, P. (2017). Urban seismology: On the origin of earth vibrations within a city. *Scientific reports*, 7(1):15296.

Ekström, G. (2014). Love and Rayleigh phase-velocity maps, 5–40 s, of the western and central USA from USArray data. *Earth and Planetary Science Letters*, 402:42–49.

Ekström, G., Abers, G. A., and Webb, S. C. (2009). Determination of surface-wave phase velocities across USArray from noise and Aki's spectral formulation. *Geophysical Research Letters*, 36(18).

El Haber, E., Cornou, C., Jongmans, D., Abdelmassih, D. Y., Lopez-Caballero, F., and Al-Bittar, T. (2019). Influence of 2D heterogeneous elastic soil properties on surface ground motion spatial variability. *Soil Dynamics and Earthquake Engineering*, 123:75–90.

Garofalo, F., Foti, S., Hollender, F., Bard, P., Cornou, C., Cox, B., Dechamp, A., Ohrnberger, M., Perron, V., Sicilia, D., et al. (2016). InterPACIFIC project: Comparison of invasive and non-invasive methods for seismic site characterization. Part II: Inter-comparison between surface-wave and borehole methods. *Soil Dynamics and Earthquake Engineering*, 82:241–254.

Green, R. A., Cubrinovski, M., Cox, B., Wood, C., Wotherspoon, L., Bradley, B., and Maurer, B. (2014). Select liquefaction case histories from the 2010–2011 Canterbury earthquake sequence. *Earthquake Spectra*, 30(1):131–153.

Hallal, M. M. and Cox, B. R. (2023). What Spatial Area Influences Seismic Site Response: Insights Gained from Multiazimuthal 2D Ground Response Analyses at the Treasure Island Downhole Array. *Journal of Geotechnical and Geoenvironmental Engineering*, 149(1):04022124.

Harkrider, D. G. (1964). Surface waves in multilayered elastic media I. Rayleigh and Love waves from buried sources in a multilayered elastic half-space. *Bulletin of the Seismological Society of America*, 54(2):627–679.

Hashash, Y. M. and Park, D. (2001). Non-linear one-dimensional seismic ground motion propagation in the Mississippi embayment. *Engineering Geology*, 62(1-3):185–206.

Hashash, Y. M. and Park, D. (2002). Viscous damping formulation and high frequency motion propagation in non-linear site response analysis. *Soil Dynamics and Earthquake Engineering*, 22(7):611–624.

Holzer, T. L., Bennett, M. J., Ponti, D. J., and Tinsley III, J. C. (1999). Liquefaction and soil failure during 1994 northridge earthquake. *Journal of Geotechnical and Geoenvironmental Engineering*, 125(6):438–452.

Hu, J. (2023). Empirical relationships between earthquake magnitude and maximum distance based on the extended global liquefaction-induced damage cases. *Acta Geotechnica*, 18(4):2081–2095.

Huang, D., Wang, G., Du, C., and Jin, F. (2021). Seismic amplification of soil ground with spatially varying shear wave velocity using 2D spectral element method. *Journal of Earthquake Engineering*, 25(14):2834–2849.

Hutabarat, D. and Bray, J. D. (2021). Effective stress analysis of liquefiable sites to estimate the severity of sediment ejecta. *Journal of Geotechnical and Geoenvironmental Engineering*, 147(5):04021024.

Inzunza, D. A., Montalva, G. A., Leyton, F., Prieto, G., and Ruiz, S. (2019). Shallow Ambient-Noise 3D Tomography in the Concepción Basin, Chile: Implications for Low-Frequency Ground Motions. *Bulletin of the Seismological Society of America*, 109(1):75–86.

Ishihara, K. (1993). Liquefaction and flow failure during earthquakes. *Geotechnique*, 43(3):351–451.

Joyner, W. B. and Chen, A. T. (1975). Calculation of nonlinear ground response in earthquakes. *Bulletin of the Seismological Society of America*, 65(5):1315–1336.

Kayen, R., Moss, R., Thompson, E., Seed, R., Cetin, K., Der Kiureghian, A., Tanaka, Y., and Tokimatsu, K. (2013). Shear-wave velocity–based probabilistic and deterministic assessment of seismic soil liquefaction potential. *Journal of Geotechnical and Geoenvironmental Engineering*, 139(3):407.

Khosravifar, A., Elgamal, A., Lu, J., and Li, J. (2018). A 3D model for earthquake-induced liquefaction triggering and post-liquefaction response. *Soil Dynamics and Earthquake Engineering*, 110:43–52.

Kissling, E. (1988). Geotomography with local earthquake data. *Reviews of Geophysics*, 26(4):659–698.

Lay, T. (2011). A chilean surprise. *Nature*, 471(7337):174–175.

Lobkis, O. I. and Weaver, R. L. (2001). On the emergence of the green's function in the correlations of a diffuse field. *The Journal of the Acoustical Society of America*, 110(6):3011–3017.

Luque, R. and Bray, J. D. (2017). Dynamic analyses of two buildings founded on liquefiable soils during the Canterbury earthquake sequence. *Journal of Geotechnical and Geoenvironmental Engineering*, 143(9):04017067.

Luque, R. and Bray, J. D. (2020). Dynamic soil-structure interaction analyses of two important structures affected by liquefaction during the Canterbury earthquake sequence. *Soil Dynamics and Earthquake Engineering*, 133:106026.

Lysmer, J. and Kuhlemeyer, R. L. (1969). Finite dynamic model for infinite media. *Journal of the Engineering Mechanics Division*, 95(4):859–877.

McGann, C. R., Arduino, P., and Mackenzie-Helnwein, P. (2012). Stabilized single-point 4-node quadrilateral element for dynamic analysis of fluid saturated porous media. *Acta Geotechnica*, 7:297–311.

McKenna, F. (2011). OpenSees: a framework for earthquake engineering simulation. *Computing in Science & Engineering*, 13(4):58–66.

Menke, W. and Jin, G. (2015). Waveform fitting of cross spectra to determine phase velocity using Aki's formula. *Bulletin of the Seismological Society of America*, 105(3):1619–1627.

Montalva, G., Ruz, F., Escribano, D., Bastías, N., Espinoza, D., and Paredes, F. (2022). Chilean liquefaction case history database. *Earthquake Spectra*, 38(3):2260–2280.

Montalva, G. A., Bastías, N., and Rodriguez-Marek, A. (2017). Ground-motion prediction equation for the Chilean subduction zone. *Bulletin of the Seismological Society of America*, 107(2):901–911.

Montalva, G. A., Chávez-Garcia, F. J., Tassara, A., and Jara Weisser, D. M. (2016). Site effects and building damage characterization in Concepción after the Mw 8.8 Maule earthquake. *Earthquake Spectra*, 32(3):1469–1488.

Montgomery, J. and Boulanger, R. W. (2017). Effects of spatial variability on liquefaction-induced settlement and lateral spreading. *Journal of Geotechnical and Geoenvironmental Engineering*, 143(1):04016086.

Moreno, M., Rosenau, M., and Oncken, O. (2010). 2010 Maule earthquake slip correlates with pre-seismic locking of Andean subduction zone. *Nature*, 467(7312):198–202.

Nelder, J. A. and Mead, R. (1965). A simplex method for function minimization. *The computer journal*, 7(4):308–313.

Newmark, N. M. (1959). A method of computation for structural dynamics. *Journal of the engineering mechanics division*, 85(3):67–94.

Ohori, M., Nobata, A., and Wakamatsu, K. (2002). A comparison of ESAC and FK methods of estimating phase velocity using arbitrarily shaped microtremor arrays. *Bulletin of the Seismological Society of America*, 92(6):2323–2332.

Olivar-Castaño, A., Pilz, M., Pedreira, D., Pulgar, J., Díaz-González, A., and González-Cortina, J. M. (2020). Regional Crustal Imaging by Inversion of Multimode Rayleigh Wave Dispersion Curves Measured From Seismic Noise: Application to the Basque-Cantabrian Zone (N Spain). *Journal of Geophysical Research: Solid Earth*, 125(12):e2020JB019559.

Parolai, S., Picozzi, M., Richwalski, S., and Milkereit, C. (2005). Joint inversion of phase velocity dispersion and H/V ratio curves from seismic noise recordings using a genetic algorithm, considering higher modes. *Geophysical Research Letters*, 32(1).

Parra-Colmenares, E. J. (1996). *Numerical modeling of liquefaction and lateral ground deformation including cyclic mobility and dilation response in soil systems*. Rensselaer Polytechnic Institute.

Petracca, M., Candeloro, F., and Camata, G. (2017). STKO user manual. *ASDEA Software Technology: Pescara, Italy*, 551.

Picozzi, M., Parolai, S., Bindi, D., and Strollo, A. (2009). Characterization of shallow geology by high-frequency seismic noise tomography. *Geophysical Journal International*, 176(1):164–174.

Pilz, M. and Cotton, F. (2019). Does the one-dimensional assumption hold for site response analysis? A study of seismic site responses and implication for ground motion assessment using KiK-net strong-motion data. *Earthquake Spectra*, 35(2):883–905.

Pilz, M., Cotton, F., and Zhu, C. (2021). How much are sites affected by two-and three-dimensional site effects? A study based on single-station earthquake records and implications for ground motion modelling. *Geophysical Journal International*.

Pilz, M., Parolai, S., Picozzi, M., and Bindi, D. (2012). Three-dimensional shear wave velocity imaging by ambient seismic noise tomography. *Geophysical Journal International*, 189(1):501–512.

Pilz, M., Parolai, S., and Woith, H. (2017). A 3-D algorithm based on the combined inversion of Rayleigh and Love waves for imaging and monitoring of shallow structures. *Geophysical Journal International*, 209(1):152–166.

Popescu, R., Prévost, J. H., and Deodatis, G. (1997). Effects of spatial variability on soil liquefaction: some design recommendations. *Geotechnique*, 47(5):1019–1036.

Popescu, R., Prevost, J.-H., and Deodatis, G. (2005). 3D effects in seismic liquefaction of stochastically variable soil deposits. *Geotechnique*, 55(1):21–31.

Popescu, R., Prevost, J. H., Deodatis, G., and Chakrabortty, P. (2006). Dynamics of nonlinear porous media with applications to soil liquefaction. *Soil Dynamics and*

*Earthquake Engineering*, 26(6-7):648–665.

Pretell, R., Ziotopoulou, K., and Abrahamson, N. (2019). Methodology for the development of input motions for nonlinear deformation analyses. In *Earthquake Geotechnical Engineering for Protection and Development of Environment and Constructions*, pages 4564–4571. CRC Press.

Pretell, R., Ziotopoulou, K., and Davis, C. A. (2021). Liquefaction and cyclic softening at Balboa Boulevard during the 1994 Northridge Earthquake. *Journal of Geotechnical and Geoenvironmental Engineering*, 147(2):05020014.

Qiu, Z., Prabhakaran, A., and Elgamal, A. (2023). A three-dimensional multi-surface plasticity soil model for seismically-induced liquefaction and earthquake loading applications. *Acta Geotechnica*, pages 1–24.

Ramirez, J., Barrero, A. R., Chen, L., Dashti, S., Ghofrani, A., Taiebat, M., and Arduino, P. (2018). Site response in a layered liquefiable deposit: evaluation of different numerical tools and methodologies with centrifuge experimental results. *Journal of Geotechnical and Geoenvironmental Engineering*, 144(10):04018073.

Ritzwoller, M. H., Lin, F.-C., and Shen, W. (2011). Ambient noise tomography with a large seismic array. *Comptes Rendus Geoscience*, 343(8-9):558–570.

Ruegg, J., Rudloff, A., Vigny, C., Madariaga, R., De Chabalier, J., Campos, J., Kausel, E., Barrientos, S., and Dimitrov, D. (2009). Interseismic strain accumulation measured by GPS in the seismic gap between Constitución and Concepción in Chile. *Physics of the Earth and Planetary Interiors*, 175(1-2):78–85.

Saldaña Sotelo, H. (2023). *Modelamiento numérico de asentamientos inducidos por licuación en la zona subductiva chilena*. Master thesis, University of Concepcion.

Saldaña, H., Montalva, G., Escribano, D., Núñez-Jara, S., and Tiznado, J. C. (2023). Two-Dimensional Nonlinear Dynamic Analysis of a Liquefaction Case History Considering Spatial Variability, and Long-Duration Megathrust Earthquakes. *Soil Dynamics and Earthquake Engineering (submitted for review)*.

Scott, M. H. and Fenves, G. L. (2010). Krylov subspace accelerated newton algorithm: application to dynamic progressive collapse simulation of frames. *Journal of Structural Engineering*, 136(5):473–480.

Seed, H. B. and Idriss, I. M. (1971). Simplified procedure for evaluating soil liquefaction potential. *Journal of the Soil Mechanics and Foundations division*, 97(9):1249–1273.

Shapiro, N. M. and Campillo, M. (2004). Emergence of broadband Rayleigh waves from correlations of the ambient seismic noise. *Geophysical Research Letters*, 31(7).

Shapiro, N. M., Campillo, M., Stehly, L., and Ritzwoller, M. H. (2005). High-resolution surface-wave tomography from ambient seismic noise. *Science*, 307(5715):1615–1618.

Taftsoglou, M., Valkaniotis, S., Papathanassiou, G., and Karantanellis, E. (2023). Satellite imagery for rapid detection of liquefaction surface manifestations: the case study of Türkiye–Syria 2023 earthquakes. *Remote Sensing*, 15(17):4190.

Tao, Y. and Rathje, E. (2020). Taxonomy for evaluating the site-specific applicability of one-dimensional ground response analysis. *Soil Dynamics and Earthquake Engineering*, 128:105865.

Thompson, E. M., Baise, L. G., Tanaka, Y., and Kayen, R. E. (2012). A taxonomy of site response complexity. *Soil Dynamics and Earthquake Engineering*, 41:32–43.

Tiznado, J. C., Dashti, S., and Ledezma, C. (2021). Probabilistic predictive model for liquefaction triggering in layered sites improved with dense granular columns. *Journal of Geotechnical and Geoenvironmental Engineering*, 147(10):04021100.

Tokimatsu, K., Tamura, S., and Kojima, H. (1992). Effects of multiple modes on Rayleigh wave dispersion characteristics. *Journal of geotechnical engineering*, 118(10):1529–1543.

Tokimatsu, K. and Uchida, A. (1990). Correlation between liquefaction resistance and shear wave velocity. *Soils and foundations*, 30(2):33–42.

Tsai, V. C. and Moschetti, M. P. (2010). An explicit relationship between time-domain noise correlation and spatial autocorrelation (SPAC) results. *Geophysical Journal International*, 182(1):454–460.

Van Ballegooy, S., Malan, P., Lacrosse, V., Jacka, M., Cubrinovski, M., Bray, J., O'Rourke, T., Crawford, S., and Cowan, H. (2014). Assessment of liquefaction-induced land damage for residential Christchurch. *Earthquake Spectra*, 30(1):31–55.

Vantassel, J. P. and Cox, B. R. (2021). SWinvert: a workflow for performing rigorous 1-D surface wave inversions. *Geophysical Journal International*, 224(2):1141–1156.

Verdugo, R. and González, J. (2015). Liquefaction-induced ground damages during the 2010 Chile earthquake. *Soil Dynamics and Earthquake Engineering*, 79:280–295.

Wapenaar, K., Slob, E., Snieder, R., and Curtis, A. (2010). Tutorial on seismic interferometry: Part 2—Underlying theory and new advances. *Geophysics*, 75(5):75A211–75A227.

Ward, K. M., Porter, R. C., Zandt, G., Beck, S. L., Wagner, L. S., Minaya, E., and Tavera, H. (2013). Ambient noise tomography across the Central Andes. *Geophysical Journal International*, 194(3):1559–1573.

Weaver, R. L. (1982). On diffuse waves in solid media. *The Journal of the Acoustical Society of America*, 71(6):1608–1609.

Welch, P. (1967). The use of fast Fourier transform for the estimation of power spectra: a method based on time averaging over short, modified periodograms. *IEEE Transactions on audio and electroacoustics*, 15(2):70–73.

Xu, Y., Lebedev, S., Meier, T., Bonadio, R., and Bean, C. J. (2021). Optimized workflows for high-frequency seismic interferometry using dense arrays. *Geophysical Journal International*, 227(2):875–897.

Yamanaka, H. and Ishida, H. (1996). Application of genetic algorithms to an inversion of surface-wave dispersion data. *Bulletin of the Seismological Society of America*, 86(2):436–444.

Yang, Z., Elgamal, A., and Parra, E. (2003). Computational model for cyclic mobility and associated shear deformation. *Journal of Geotechnical and Geoenvironmental Engineering*, 129(12):1119–1127.

Youd, T. L. and Idriss, I. M. (2001). Liquefaction resistance of soils: summary report from the 1996 NCEER and 1998 NCEER/NSF workshops on evaluation of liquefaction resistance of soils. *Journal of geotechnical and geoenvironmental engineering*, 127(4):297–313.

Zhang, J. and Wang, Y. (2021). An ensemble method to improve prediction of earthquake-induced soil liquefaction: a multi-dataset study. *Neural Computing and*

*Applications*, 33:1533–1546.

Zhang, Y., Xie, Y., Zhang, Y., Qiu, J., and Wu, S. (2021). The adoption of deep neural network (DNN) to the prediction of soil liquefaction based on shear wave velocity. *Bulletin of Engineering Geology and the Environment*, 80:5053–5060.

Zhou, Y.-G. and Chen, Y.-M. (2007). Laboratory investigation on assessing liquefaction resistance of sandy soils by shear wave velocity. *Journal of Geotechnical and Geoenvironmental Engineering*, 133(8):959–972.

Zienkiewicz, O. and Shiomi, T. (1984). Dynamic behaviour of saturated porous media; the generalized Biot formulation and its numerical solution. *International journal for numerical and analytical methods in geomechanics*, 8(1):71–96.

# Supplemental Material

## S1 Scientific Production

From the development of this Thesis, a scientific manuscript - bearing the same title as the thesis - was produced and submitted to the journal *Frontiers in Earth Science*, in the frame of the research topic *Near-Surface Geophysics in Latin American Contexts: Its applications, Education and Societal Perspectives as a whole*. The manuscript is currently in the peer-review process. We acknowledge the co-authors Dr. Gonzalo Montalva, Dr Marco Pilz, Dr. Matt Miller, Héctor Saldaña, Dr. Andrés Olivar-Castaño and Dr. Rodolfo Araya for their contributions in both the manuscript and the thesis. If published, the manuscript will be available under open access and will be searchable in the usual databases and search engines.

# S2 Supplemental Figures

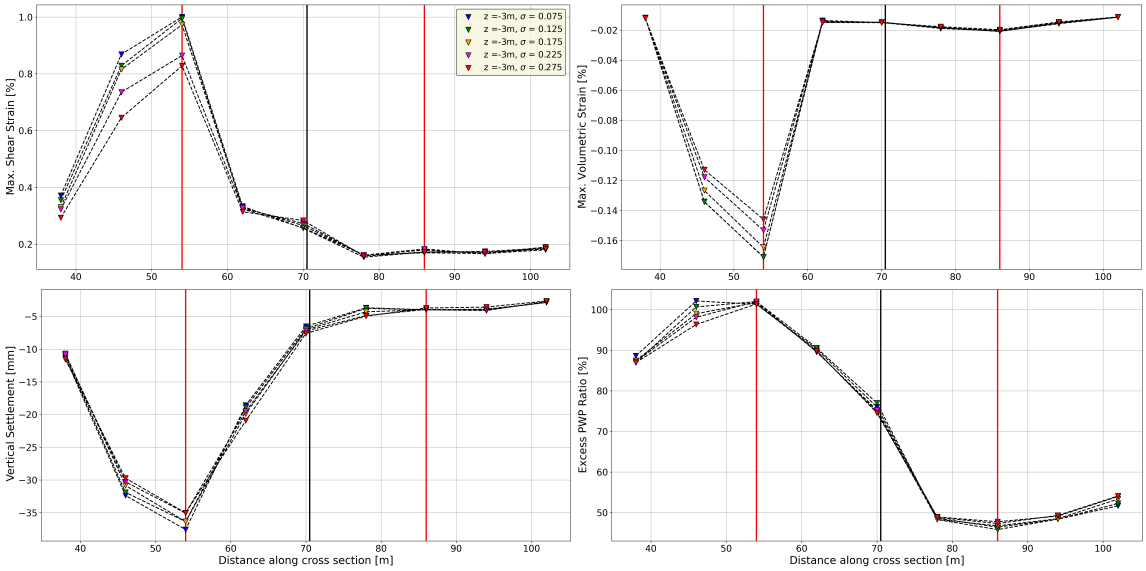


**Figure S2.1:** The same parameters, represented in the same colors, as for Fig. 4.2.1, but this time for a depth of 3 meters.

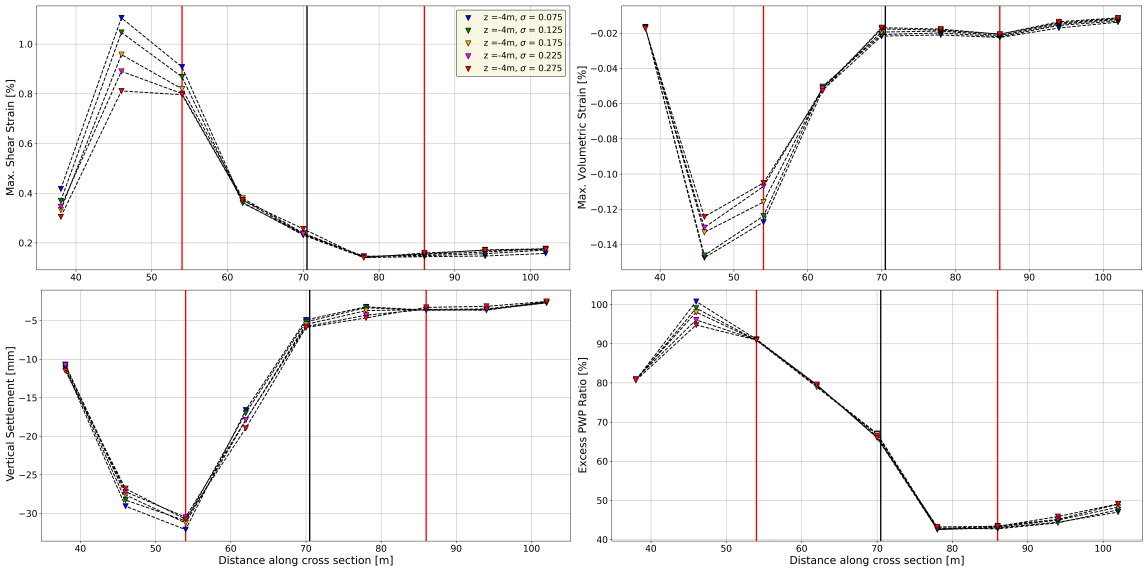


**Figure S2.2:** The same parameters, represented in the same colors, as for Fig. 4.2.1, but this time for a depth of 4 meters.

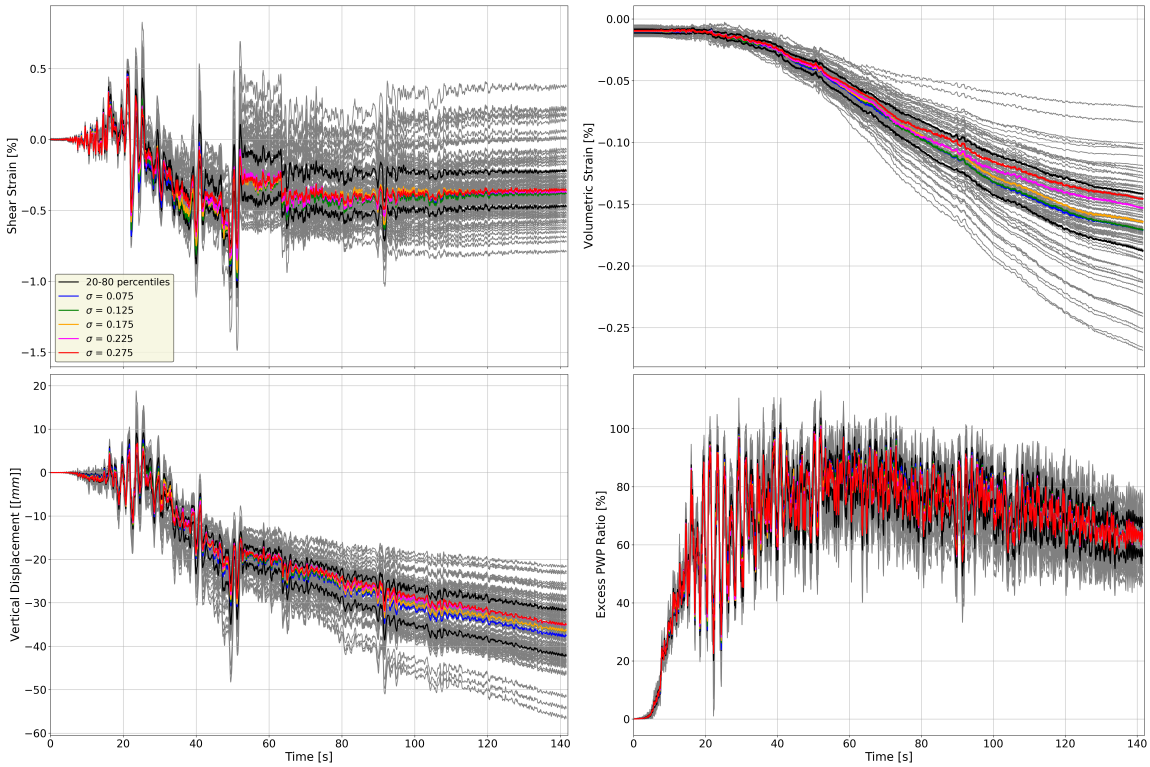


**Figure S2.3:** The same parameters, represented in the same colors, as for Fig. 4.2.2, but this time for the western node at position $x = 54$ at a depth of 3 meters.

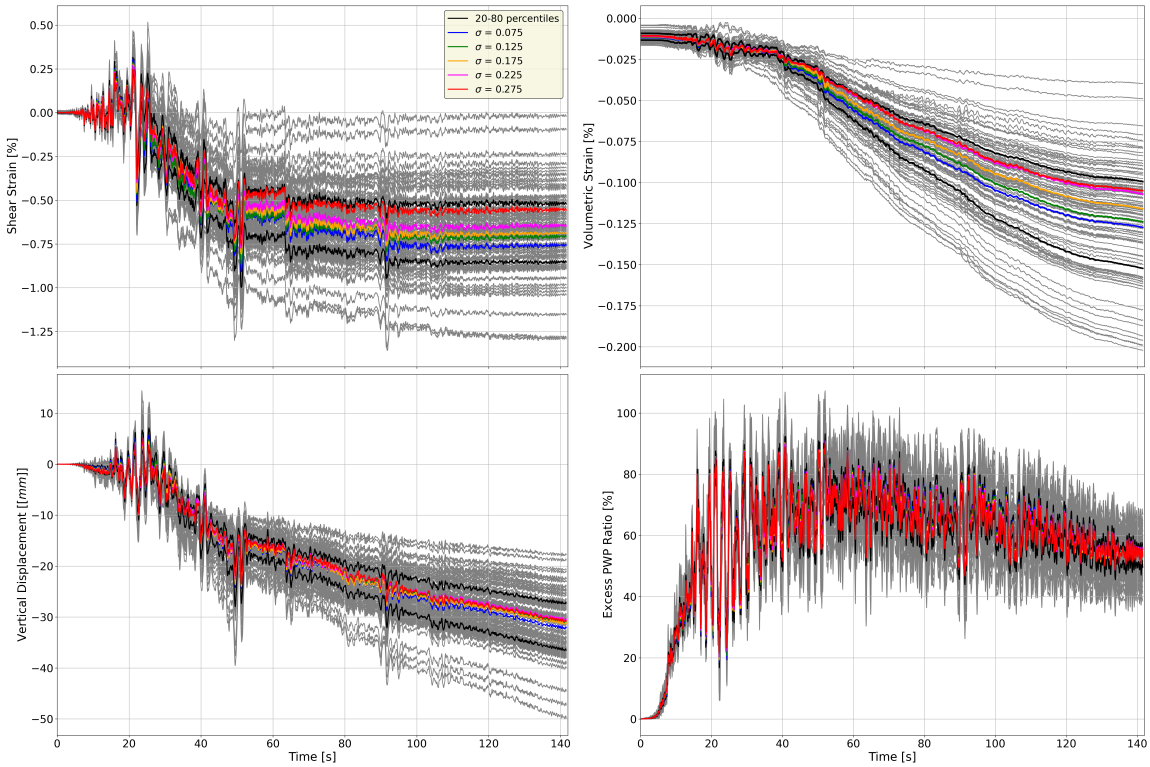


**Figure S2.4:** The same parameters, represented in the same colors, as for Fig. 4.2.2, but this time for the western node at position $x = 54$ at a depth of 4 meters.

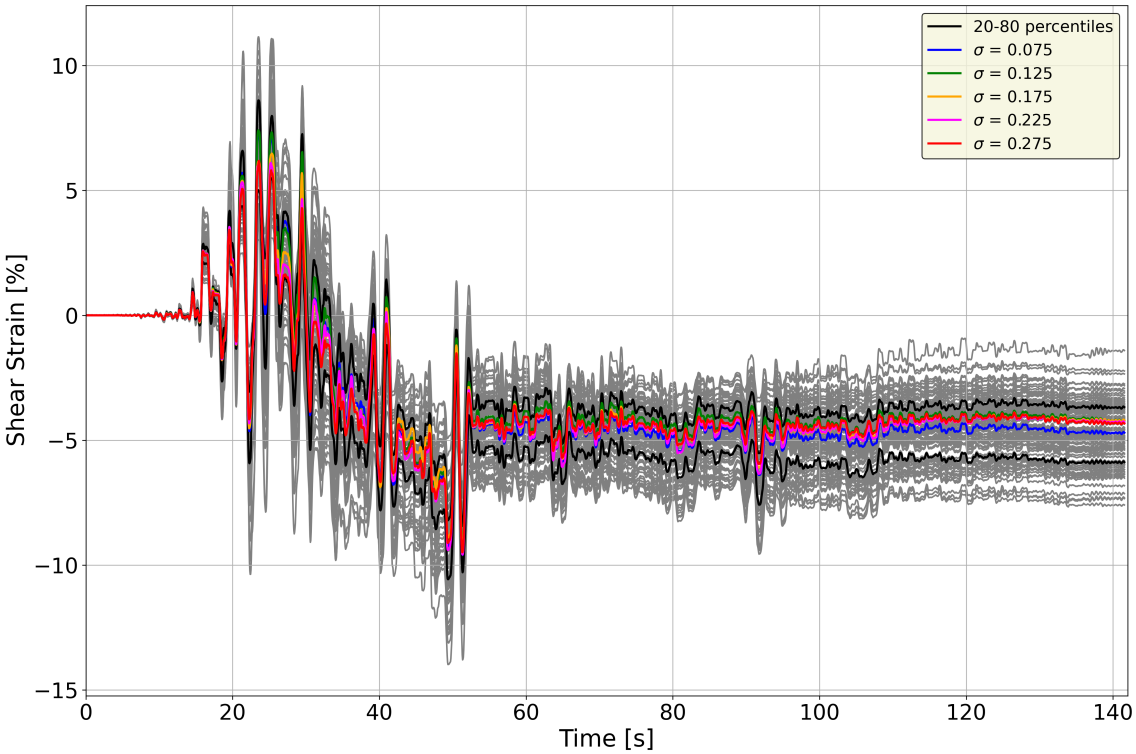


**Figure S2.5:** The same parameters, represented in the same colors, as for Fig. 4.2.2, but this time for the eastern node at position $x = 86$ and depth of 2 meters.